Imaging of live bacterial whole-cell biosensors illuminates spatial sialic acid availability within the inflamed mammalian gut.

David Carreño [1, 2], Clare M Robinson [1, 2, †], Raphaella Jackson [1, ‡], Peirong Li [1], Vanessa Nunes [2], Susana A. Palma-Duran [2, §], Emma Nye [2] , James I. MacRae [2] and David T. Riglar [1, 2, *].

[1] Department of Infectious Disease, Imperial College London, London, UK
[2] Francis Crick Institute, London, UK
[†] Current Address: Full Circle Labs Ltd, Venture X White City, London, UK
[‡] Current Address: Department of Women and Children's Health, King's College London, UK
[§] Current Address: Department of Food Science, Research Centre in Food and Development A.C., Hermosillo, Mexico

***Correspondence: d.riglar@imperial.ac.uk**

Abstract:

Host mucin-derived sialic acids are key drivers of microbial colonisation, growth and pathogenicity within the mammalian gut. However, their study is hindered by complex spatiotemporal dynamics, with availability driven by the interplay of microbial sialidase enzyme activity and microbial utilisation. Here, we demonstrate regional increases in the bioavailability of sialic acid in the inflamed mouse gut. We monitor metabolite availability *in situ* using an engineered bacterial whole-cell biosensor colonised within the gut. Through organ-scale imaging of cleared tissues at single bacterial resolution we observe strong correlations between global inflammation status and biosensor response. Profiling along the length of the gut uncovers regional variations between the peak sialic acid sensing and the peak inflammatory response within host tissues. These data illuminate the complex spatial dynamics involved in shared host-microbiome metabolism and demonstrate the broader power of using engineered bacterial biosensors to monitor bioavailability *in situ* within the gut.

Introduction:

The metabolic and microbial contents of the mammalian gut alter in disease conditions. For example, an inflammatory gut environment has been broadly associated with increased prevalence of facultative anaerobes [1] and a decrease in microbiome-associated metabolite diversity [2]. However, quantification of various gut metabolites is complicated by their rapid depletion, reaction or reabsorption, altering local concentrations in a microbiome-dependent manner and complicating inferences that can be drawn from faecal sampling alone.

The mammalian gut represents a spatially dynamic and heterogenous environment on both longitudinal and radial axes [3]. Complex and dynamic gradients of oxygen, pH, dietary and host-derived nutrients, and antimicrobial compounds are just a few of the many factors shaping microbiome organisation and function throughout the gut. There are, differences in the relative abundances of microbial species across several broad gut niches (e.g. luminal vs mucosal-associated vs faecal microbiota) [4-10], albeit with uncertainty as to the degree of difference between each site [7,11-13]. Indeed, various microbiome-related disease signatures that are evident in biopsy samples of the mucosal-associated microbiota are not reflected in far more accessible and prevalently studied stool samples [14-16]. On a functional level, inter-microbial interaction networks are diet and gut-location dependent [17].

Mucus-derived carbohydrates are a particularly important nutrient class for microbes within the mammalian gut. The gut epithelium is protected by a layer of mucus, predominantly secreted by goblet cells. Highly glycosylated mucin proteins are a key component of this mucus, with MUC2 the dominant protein in both mouse and human [18,19]. Variation in expression levels and the glycosylation patterns that decorate mucin proteins occurs throughout the gut, leading to structural and functional differences in mucus and altering its interactions with the gut microbiota [20]. One key difference is the terminal monosaccharide of the glycosylation chain, which is typically either a sialic acid or fucose. While the sialic acid family includes many derivatives of the 9-carbon monosaccharide, the most abundant is N-acetylneuraminic acid (Neu5Ac). Data are limited but opposing gradients of sialylation and fucosylation are reported along the length of the colon in humans and mice [21,22].

Sialic acid monosaccharides can be liberated from mucin glycoproteins by microbial- and host-derived sialidase enzymes (Figure 1A). While some bacterial species encode genes for both sialidases to release the monosaccharide and sialic acid catabolism to use it (eg. *Akkermansia*

muciniphila), others typically express only sialidase (eg. *Bacteroides thetaiotaomicron* and *Phocaeicola vulgatus*) or catabolic gene repertoires (eg. *Escherichia coli* and various pathogenic species [23-26]). In some pathogens, sialyltransferases also facilitate surface exposure of sialic acid and immune evasion [27]. Thus, it appears free sialic acid acts as a community resource that can be used by various species within the gut (Figure 1A). Increased MUC2 expression and increased levels of sialidase-encoding species have been associated with inflammatory disease. For example, sialidase inhibition or knock-out of the α-2,3 sialyltransferase *St3gal4* reduces inflammation and perturbations to the microbiome otherwise caused by a dextran sulfate sodium (DSS) mouse inflammation model [28]. Huang and colleagues inferred that increased free sialic acid availability led to increased growth and persistence of *E. coli* bacteria within the gut, potentiating the downstream inflammatory phenotypes [28]. However, direct quantification of sialic acid within the gut did not detect increases, likely due to rapid catabolism by the gut microbiota.

Sialic acid availability modulates gene expression of a range of genes, including induction of those central to sialic acid catabolism, in various bacterial species. In *E. coli,* sialoregulon expression is controlled by the transcriptional regulator NanR [29]. NanR represses gene expression of several regulated operons, with direct binding by Neu5Ac leading to derepression and gene expression [30]. In *Citrobacter rodentium,* sialic acid can also induce pathogenicity [31]. On a biotechnology level, sialic acid was recently used to regulate a 'sense-and-respond' therapeutic engineered in *E. coli* bacteria through the *nanA* gene promoter [32]. While the overall importance of sialic acid and sialidase activity is clear, there remains limited understanding of the spatial dynamics of this complex system.

Our group and others have demonstrated the power of engineered bacterial transcriptional reporters as robust, sensitive biosensors of the gut environment. Here, we combine the development of one such biosensor induced by sialic acid with imaging advances to assess its activity across organ-level scales within the gut. Assessing reporter activity in a mouse DSS inflammation model, in the presence and absence of sialidase inhibition, we demonstrate disease-specific biosensing. Spatial analysis affords insights into regional sialic acid availability within the colon. The understanding gained illuminates previously unexplored spatial distinctions between the availability of this key metabolite and inflammatory phenotypes within the gut.

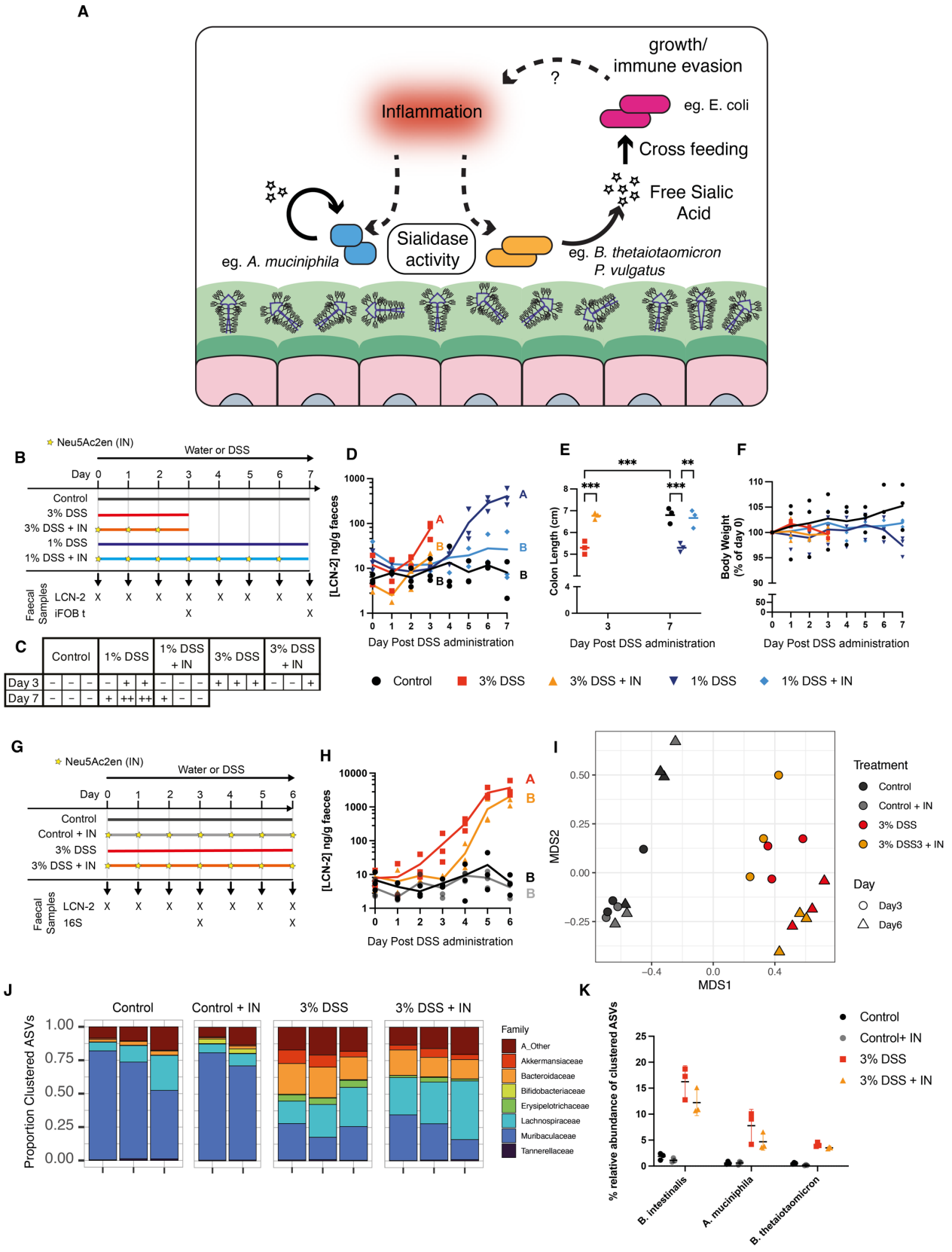
A
growth/
immune evasion
?
Inflammation
eg. E. coli
Cross feeding
Free Sialic
Acid
Sialidase
activity
eg. A. muciniphila
eg. B. thetaiotaomicron
P. vulgatus
B
Neu5Ac2en (IN)
Water or DSS
Day 0 1 2 3 4 5 6 7
Control
3% DSS
3% DSS + IN
1% DSS
1% DSS + IN
Faecal Samples
LCN-2 X X X X X X X X
iFOB t X X
C
Control
1% DSS
1% DSS + IN
3% DSS
3% DSS + IN
Day 3 – – – – + + – – – + + + – – +
Day 7 – – – + ++ ++ + – –
D
[LCN-2] ng/g faeces
Day Post DSS administration
E
Colon Length (cm)
Day Post DSS administration
F
Body Weight (% of day 0)
Day Post DSS administration
Control
3% DSS
3% DSS + IN
1% DSS
1% DSS + IN
G
Neu5Ac2en (IN)
Water or DSS
Day 0 1 2 3 4 5 6
Control
Control + IN
3% DSS
3% DSS + IN
Faecal Samples
LCN-2 X X X X X X X
16S X X
H
[LCN-2] ng/g faeces
Day Post DSS administration
I
MDS2
MDS1
Treatment
Control
Control + IN
3% DSS
3% DSS3 + IN
Day
Day3
Day6
J
Proportion Clustered ASVs
Control
Control + IN
3% DSS
3% DSS + IN
Family
A_Other
Akkermansiaceae
Bacteroidaceae
Bifidobacteriaceae
Erysipelotrichaceae
Lachnospiraceae
Muribaculaceae
Tannerellaceae
K
% relative abundance of clustered ASVs
B. intestinalis
A. muciniphila
B. thetaiotaomicron
Control
Control+ IN
3% DSS
3% DSS + IN

Figure 1. The impacts of sialidase inhibition in a DSS induced colitis mouse model. A) Schematic of the current knowledge of sialic acid bioavailability within the gut. Bacterial sialidase enzymes catalyse the release of sialic acid monosaccharides from gut mucin glycoproteins. Free sialic acid in the gut can be utilised by a range of microbes, including *E. coli*, via cross-feeding. Increases in both sialidase encoding and sialic acid catabolising strains have been associated with inflammatory phenotypes**.** B) DSS at 3%, 1%, or 0% (control) was administered to C57BL/6 mice (n=3 per group) in the drinking water for a period of 3 (3% group) or 7 (1% group) days. To repress sialidase activity, some animals also received daily Neu5Ac2en sialidase inhibitor (IN) via oral gavage (stars). C) Faecal occult blood test (iFOB t) results from day 3 and 7. Absence (-) and presence of low (+) to high (++) levels of colorimetric change are indicated. D) LCN-2 levels as quantified by indirect ELISA of faecal pellets. Lines show mean. Statistics were calculated by one-way ANOVA with Tukey multiple comparison correction on AUC to day 3 (3% DSS groups and control) or day 7 (1% DSS groups and control). Different compact letter (A-B) indicates significant differences between means. E) Colon length as measured at the experimental endpoint on day 3 or 7. Line shows mean and statistics calculated by one-way ANOVA with Šídák multiple comparison correction. Adjusted p values are indicated *=p <0.05, **=p <0.005, ***=p <0.001. F) Body weight change, expressed as a percentage of starting body weight of each mouse. Line shows mean. G) DSS was administered in the drinking water of C57BL/6 mice (n=3 per group) at 0% (control) or 3% with or without daily oral gavage of Neu5Ac2en sialidase inhibitor (IN; stars). H) LCN-2 levels quantified by indirect ELISA of faecal pellets. Lines show mean. Statistics were calculated by one-way ANOVA with Tukey multiple comparison correction on AUC. Different compact letter (A-B) indicates significant differences between means. I) Multidimensional scaling of 16s rRNA sequencing data from faecal pellets at day 3 and 6 using monoMDS. Distance based on Bray Curtis, stress 0.0457. J) Proportion of bacterial clustered ASVs within a family taxonomic classification at day 3. K) Percentage of relative abundance of clustered ASVs that showed similarity (over 97%) with those of *B. intestinalis*, *A. muciniphila* and *B. thetaiotaomicron* at day 3.

Results:

Sialidase activity contributes to colitis development in a mouse inflammation model

Microbiota-derived sialidase activity has been linked to alterations in inflammation and microbiome composition in a dextran sodium sulphate (DSS)-induced inflammation model [28]. To confirm the impact of sialidases on inflammation, we administered DSS (3%, 1%, or control) to C57BL/6 mice (n=3 per experimental group) in their drinking water for a period of 3 (3% group) or 7 (1% group) days (Figure 1B). To inhibit sialidase activity, some animals also received Neu5Ac2en sialidase inhibitor (IN) [33] via daily oral gavage (Figure 1B). Disease progression was monitored daily via faecal sampling, and via colon dissection at the experimental endpoint. Under both regimes, DSS provision led to increased inflammation, as evidenced by higher levels of faecal occult blood (Figure 1C), increased levels of the inflammatory biomarker lipocalin-2 (LCN-2) in faeces (Figure 1D), and decreased colon length upon dissection (Figure 1E). These impacts from DSS were significantly mitigated by concurrent sialidase inhibition (Figure 1C-E); results from both the 3%

DSS + IN group at day 3 and 1% DSS + IN group at day 7 were indistinct from those of controls. DSS treated animals also showed some evidence of decreased weight compared to controls, as expected in this model, albeit without statistical significance over the short timeframe and low dose regimes tested (Figure 1F). Together these data confirm the importance of sialidase activity for inflammation in this model.

Additional testing of control and 3% DSS treated animals (n=3 per group), with or without daily Neu5Ac2en sialidase inhibitor for 6 days, further confirmed the ability for sialidase inhibition to delay inflammation in this model (Figure 1G). 3% DSS + IN treated animals again showed significantly lower LCN-2 measured across the course of the 6-day experiment than 3% DSS alone as measured by one way ANOVA test between area under the curve (P=0.034); values were statistically indistinct from control (P=0.279) and control + IN animals (P=0.273), however, levels were notably increased by day 6 of the experiment (Figure 1H). To assess impacts on microbiome composition, 16s ribosomal RNA (rRNA) sequences were analysed from faecal samples at day 3 and 6 post administration (Figure 1G). Long-read PacBio sequencing of the full 16s rRNA region followed by amplicon sequence variant (ASV) identification and clustering showed distinct microbiome compositions in DSS treated groups compared to controls, including sialidase inhibitor treated animals (Figure 1I; Pr(>F): 0.003). Differences were predominantly driven by bacterial families that have previously been associated with inflammation and DSS treatment, including increases in relative abundance of *Akkermansiacea and Bacteroidaceae* and decreases in *Muribaculaceae* (Figure 1J, Supplementary Fig 1A). Our data were unable to distinguish between the presence or absence of sialidase inhibitor in either control (Pr(>F): 0.25) or DSS treatment groups (Pr(>F): 0.242).

Development of a live bacterial bioreporter to quantify sialic acid bioavailability to the microbiome

Notably, clustered ASV's showing similarity to prominent sialidase-encoding strains such as *A. mucinophila, B. intestinalis and B. thetaiotaomicron* were among those that increased in relative abundance in DSS samples (Figure 1K, Supplementary Figure 1B), with *B. intestinalis and B. thetaiotaomicron* typically lacking sialic acid utilisation capacity and thus thought to increase free sialic acid availability for other community members [25].

Rapid utilisation of sialic acid by microbes could lead to underestimation of sialic acid levels when quantified by traditional methods. We therefore reasoned that a microbially-encoded

transcriptional biosensor may be a more reliable and accurate reporter of metabolite availability within the gut microbiome. To develop a sialic acid-responsive whole cell biosensor, we therefore cloned a small library of 8 putative sialic acid transcriptional reporters in the mouse commensal *E. coli* strain NGF-1 [34]. Sensors were controlled by the *E. coli* NanR gene regulator [30] and consisted of an inducible fluorescence output (mVenus) to assess sialic acid response combined with a second, constitutively expressed, fluorophore (mKate2) for engineered bacterial identification during image analysis (Figure 2A: Supplementary Figure 2A). All circuits were integrated at single copy in the genome. Despite lowering biosensor output, this design choice is expected to minimise impact of engineered circuits on the bacterial chassis and thus facilitate native growth and function within the mouse gut and reduce the likelihood of synthetic circuit mutation and loss. The single-copy design was also chosen to preserve native NanR sensitivities as closely as possible. Previous studies have noted loss of NanR regulation using plasmid-based reporter systems, presumably due to binding site titration effects [32].

The sensors tested included all *E. coli* promoter regions with predicted NanR regulation: *nanATEKQ*, *nanCMS*, *nanXY* and *fimB*. Additionally, 4 synthetic promoters previously engineered with the NanR binding motif were tested [35]. Growth of each biosensor in the presence or absence of Neu5ac (SA; 0μM, 10μM, 100μM or 1000μM) identified two sensors with notably increased fluorescence response at higher sialic acid levels (Figure 2B-C). In particular, the *E. coli nanXY* gene promoter (P_{nanX}) (strain: DTR413) showed the desired characteristics of a low biosensor output at low sialic acid concentrations (Figure 2B) and the highest proportional activation of the reporter at elevated sialic acid concentrations (Figure 2C). Induction of DTR413 at mid-log phase further demonstrated the strain's rapid response dynamics, with increased fluorescence detected as early as ~30 minutes post induction and distinction between all sialic acid concentrations tested by ~1-1.5 hours (Figure 2D). *In vitro* reporter response was not impacted by addition of the Neu5Ac2en sialidase inhibitor (Figure 2E).

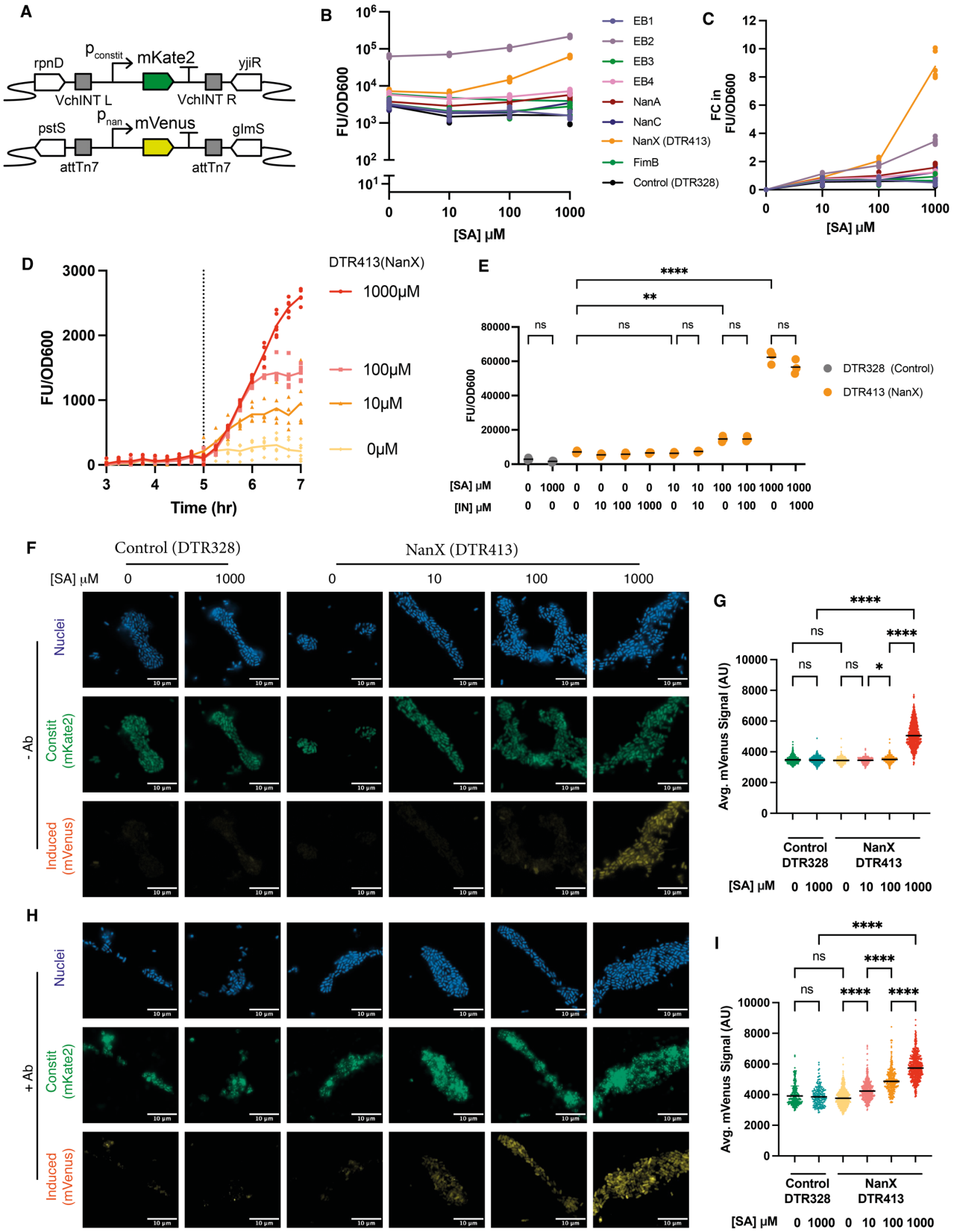
A
rpnD
$p_{constit}$
mKate2
yjiR
VchINT L
VchINT R
pstS
p_{nan}
mVenus
glmS
attTn7
attTn7
B
FU/OD600
[SA] µM
EB1
EB2
EB3
EB4
NanA
NanC
NanX (DTR413)
FimB
Control (DTR328)
C
FC in FU/OD600
[SA] µM
D
FU/OD600
Time (hr)
DTR413(NanX)
1000µM
100µM
10µM
0µM
E
FU/OD600
DTR328 (Control)
DTR413 (NanX)
[SA] µM
[IN] µM
F
Control (DTR328)
NanX (DTR413)
[SA] µM
Nuclei
Constit (mKate2)
Induced (mVenus)
- Ab
G
Avg. mVenus Signal (AU)
Control DTR328
NanX DTR413
[SA] µM
H
+ Ab
I
Avg. mVenus Signal (AU)
Control DTR328
NanX DTR413
[SA] µM

Figure 2. Development of a live bacterial whole-cell biosensor shows quantitative response to sialic acid bioavailability. A) Gene circuit construction of fluorescent sensor strain. *E. coli* NGF-1 bacteria were engineered with a constitutively expressed mKate2 fluorescent reporter, inserted into the genome between *rpnD* and *yjiR* genes. Inducible promotors predicted to be controlled by *E. coli NanR* gene regulator were cloned in front of an mVenus fluorescent reporter and inserted into the genome downstream of the *glmS* gene B) Fluorescence output normalised by OD600 at 6 hours exposed to different concentrations of Neu5Ac (SA; 0mM, 10mM, 100mM or 1000mM) in LB media) for 8 putative sialic acid biosensors and a negative control (DTR328) lacking mVenus induction. Line shows mean of 6 replicates. C) The same data from B, plotted as fold change compared to background fluorescence at 0μM Neu5Ac. Graph shows mean of 6 replicates. D) Fluorescence output of DTR413 (NanX), normalised by OD600 and DTR328 (negative control) background, following mid-growth Neu5ac induction (0μM, 10μM, 100μM or 1000μM) in M9 media + 0.4% glycerol. Graph shows mean of 6 replicates. The dotted line represents the time of Neu5Ac addition. E) Fluorescence output of DTR413(NanX) and DTR328 (negative control), normalised by OD600, at 6 hours post induction in LB media supplemented with increasing concentrations of Neu5Ac and sialidase inhibitor Neu5Ac2en (IN). Graph shows mean of 6 replicates. Statistics shown for one-way ANOVA with Šídák multiple comparison adjustment. * = $p<0.05$, **= $p<0.01$, ***p=<0.005, ****p=<0.0001. F) Widefield microscopy-based detection of native fluorescent reporter expression from DTR413 (NanX) and DTR328 (negative control) in response to the induction with increasing concentrations of Neu5Ac for 6h in LB medium. G) Average mVenus signal (AU) of segmented bacteria from F. Statistics shown for Kruskal Wallis test with Dunn's multiple comparison adjustment as measured between treatments shown. * = $p<0.05$, ****= $p<0.0001$. H) Widefield microscopy-based detection of antibody-labelled reporter response of DTR413 (NanX) and DTR328 (negative control) with the same conditions as F, above. I) Average mVenus signal (AU) on bacteria from H. Statistics as for G, above.

Microscopy-based detection of biosensor response

We next confirmed the ability to detect DTR413 reporter activation by microscopy. DTR413 bacteria were induced in sialic acid for 6 hours and imaged via widefield microscopy. Mirroring results from plate reader assays, DTR413 bacteria were induced specifically at high concentrations of sialic acid (Figure 2F). To quantify the induction, image analysis was performed on bacteria segmented using a classifier generated using Labkit software in ImageJ (Supplementary Figure 2B) [36]. Increased mVenus fluorescence levels within segmented bacteria were detectable in DTR413 bacteria at 1000μM sialic acid but not in control bacteria (DTR328), nor at lower concentrations of sialic acid (Figure 2G). mKate2 fluorescence was not impacted by sialic acid levels (Supplementary Figure 2C).

In preparation for imaging of reporter bacteria within the gut, where the combination of inconsistent oxygen levels and a highly auto-fluorescent background create challenges for direct fluorescent protein detection, we also tested the ability to detect and amplify reporter signals through indirect immunohistochemistry (Figure 2H). Fixed and permeabilised bacteria were labelled with α-GFP (mVenus), α-RFP (mKate2) and DAPI (nuclei) and imaged via widefield

microscopy. *In vitro* induced bacteria again demonstrated successful detection and amplification of reporters. Visual inspection (Figure 2H) and quantification of segmented bacteria (Figure 2I) showed increases of induced mVenus reporter at all sialic acid levels tested (>10μM) but no systematic impact on mKate2 levels (Supplementary Figure 2D). Together these data demonstrate the ability of this engineered biosensor to report on sialic acid availability.

Tissue clearance for gut microbiome imaging

A challenge for imaging-based exploration of host-microbe interactions is the difficulty of achieving consistent fixation, manipulation and imaging of gut tissue with the gut contents remaining in place. We reasoned that whole-mount imaging would be a powerful method to enable wholistic exploration of spatial interactions between host and gut contents. Tissue clearing methods have been extensively used to increase host tissue transparency enabling whole mount imaging of gut and other tissues, but the impact of clearing on gut contents and the delicate mucus layer has not been well explored.

To clear gut tissue samples with gut contents in place, we therefore optimised the clearing-enhanced 3D (Ce3D) method [37,38] for this tissue (Figure 3A). Ce3D was chosen based on its compatibility with a range of downstream imaging options including direct preservation of fluorescent proteins, dye-based labelling, immunohistochemistry and fluorescence *in situ* hybridisation (FISH) methods [38]. Ce3D cleared gut samples increased in transparency suggesting successful optical clearance of host tissue along with substantial, but incomplete, optical clearance of gut contents (Figure 3A). Imaging of optically cleared mouse colon samples co-labelled with the EUB338 FISH probe (labelling most bacterial phyla), anti-Muc2 antibody (labelling mucus), and DAPI (labelling nuclei) demonstrated preservation of gut tissue, mucus and contents and an ability to explore features of host and microbiota at single-bacterial resolution across large regions of tissue (Figure 3B).

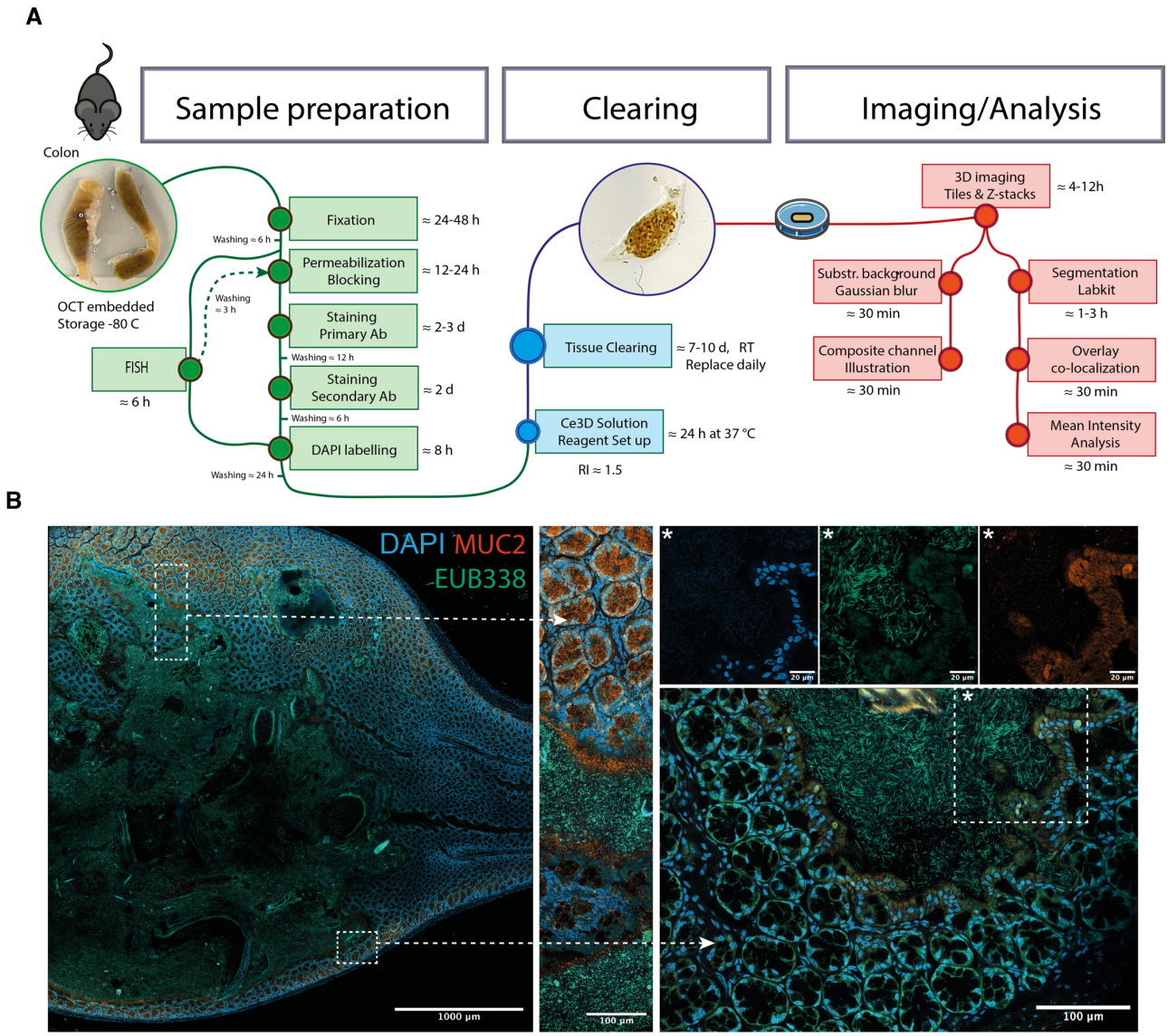

Figure 3. Clearance enhanced 3D facilitates whole-mount tissue imaging of mouse gut and gut microbiome A) Ce3D workflow from [38] adapted to mouse colon samples without gut contents removal, with options for labelling of the tissue using fluorescence *in situ* hybridisation (FISH) or indirect immunohistochemistry (IHC). B) Tile image of a Ce3D mouse colon imaged using a confocal microscopy. Labelling shows nuclei (DAPI, blue), mucus (IHC of MUC2, orange), universal bacteria (EUB338 eubacterial FISH probe, green). Scale bars as shown on image.

To further confirm our capacity to image inducible biosensor activity using this approach, we also tested a control, engineered *E. coli* NGF-1 biosensor strain with tetracycline-inducible mVenus reporter activity (P_{tetA}) (DTR326) (Supplementary Figure 3A-B). DTR326 bacteria were administered to mice by oral gavage and induced with anhydrotetracycline (aTc) or PBS (Control) (Supplementary Figure 3C). Imaging of Ce3D cleared tissue demonstrated specific induction of the mVenus reporter in animals receiving aTc (Supplementary Figure 3D-E). Together these data confirm our ability to probe bacterial gene expression *in situ* within the colon using Ce3D cleared gut tissue.

Whole-cell biosensing detects disease-induced sialic acid changes within the murine gut

We next tested the ability for DTR413 bacteria to sense sialic acid *in situ* within the mammalian gut. We have previously demonstrated the ability for engineered *E.coli* NGF-1 to colonise the murine gut at ~10^{4-5} CFU/g faeces for extended periods (likely indefinitely) when delivered 24 hours after a single, low dose of streptomycin (5mg/ mouse) [39,40]. Indeed, in pilot experiments, DTR413 reached similar steady state levels ~5 days post administration and remained at these levels for the duration of the 7-day experiment (Supplementary Figure 4A-B). *Ex vivo* testing of DTR413 colonies (72 colonies from 4 animals) after 4 days growth within murine gut also confirmed that they maintained their function in the presence and absence of DSS (Supplementary Figure 4 C-E).

DTR413 bacteria (2 x 10^{10} CFU/mouse) were therefore delivered to animals (n = 2/ group) via oral gavage following streptomycin treatment (5mg/ mouse) (Figure 4A). All animals received a low-alfalfa diet to reduce autofluorescence in the gut contents. Mice were administered DSS (3%) or normal drinking water in the presence or absence of daily Neu5Ac2en sialidase inhibitor gavages (Figure 4A). At day 4 post administration, faecal CFU counts of the engineered *E. coli* were ~10^{5-6} in all groups (Figure 4B). Consistent with previous DSS experiments, colon lengths were reduced (Figure 4C) and faecal LCN-2 levels were elevated (Figure 4D) in DSS treated animal compared to controls, with reduced impacts of DSS seen in animals co-administered with sialidase inhibitor.

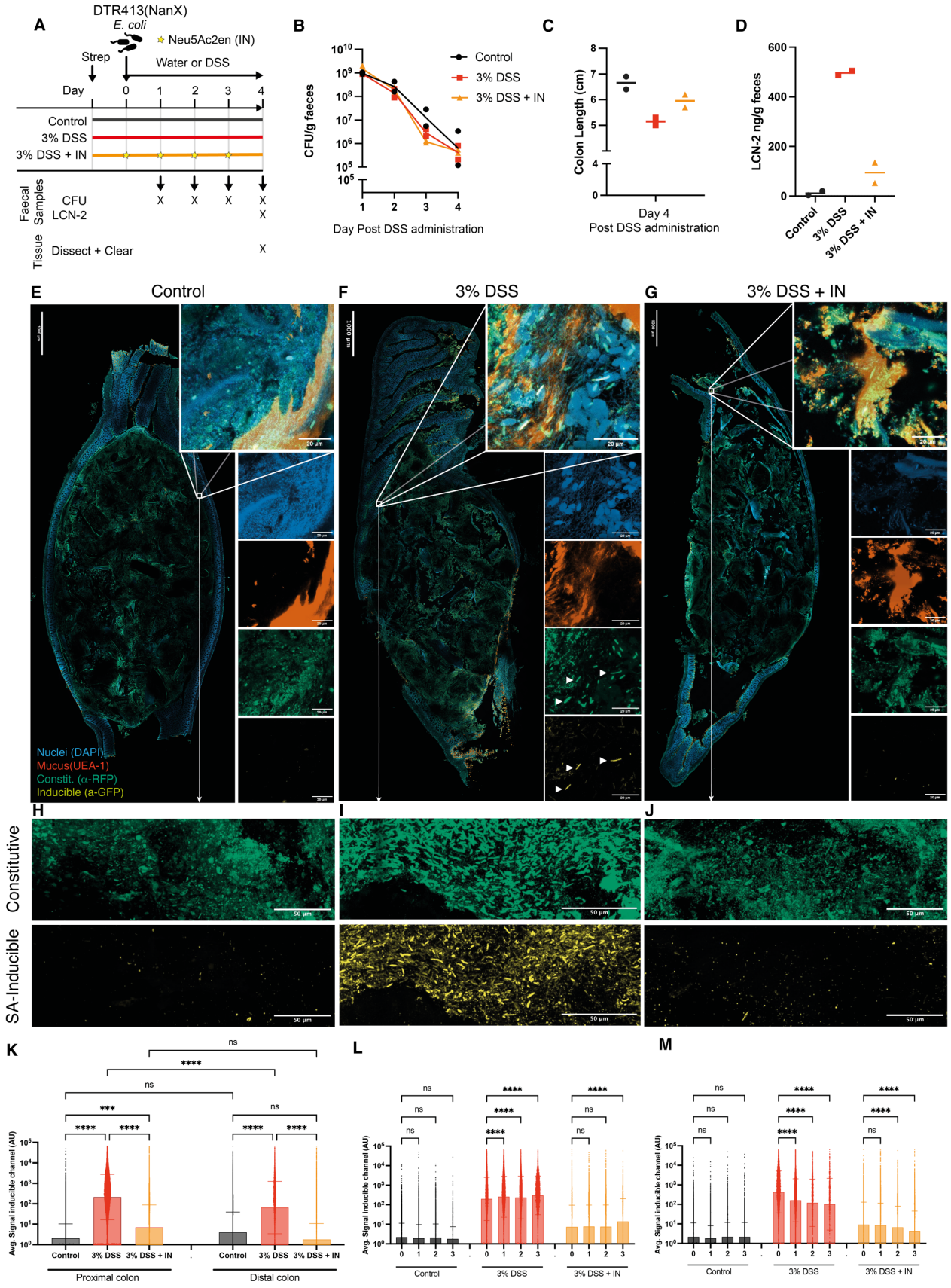
A
DTR413(NanX)
E. coli
Neu5Ac2en (IN)
Strep
Water or DSS
Day
0
1
2
3
4
Control
3% DSS
3% DSS + IN
Faecal Samples
CFU
LCN-2
Tissue
Dissect + Clear
B
CFU/g faeces
Control
3% DSS
3% DSS + IN
Day Post DSS administration
C
Colon Length (cm)
Day 4
Post DSS administration
D
LCN-2 ng/g feces
Control
3% DSS
3% DSS + IN
E
Control
F
3% DSS
G
3% DSS + IN
Nuclei (DAPI)
Mucus(UEA-1)
Constit. (α-RFP)
Inducible (a-GFP)
H
I
J
Constitutive
SA-Inducible
K
Avg. Signal inducible channel (AU)
Control
3% DSS
3% DSS + IN
Proximal colon
Distal colon
L
Avg. Signal inducible channel (AU)
Control
3% DSS
3% DSS + IN
M
Avg. Signal inducible channel (AU)
Control
3% DSS
3% DSS + IN

Figure 4. Engineered bacterial biosensor response to sialic acid as imaged in Ce3D whole mount mouse colon sections correlates with global inflammation status. A) DTR413 sialic acid-inducible whole cell biosensors were administered to C57BL/6 mice (n = 2 per group) by gavage 24 hours following a single dose of streptomycin (5mg per mouse by oral gavage). DSS was administered from the day of bacterial delivery in the drinking water at 0% (control) and 3% with or without daily oral gavage of Neu5Ac2en sialidase inhibitor (IN; stars). B) DTR413 bacterial levels were tracked daily in faecal pellets. Graph shows mean. C) Colon length at experimental endpoint. Graph shows mean. D) LCN-2 levels quantified by indirect ELISA in faecal pellets collected at day 4. Graph shows mean. E-G) Tiled confocal imaging of whole mount, Ce3D cleared proximal colon samples from Control (E), 3% DSS (F) and 3% DSS + IN (G) treated animals. Samples were IHC labelled for induced mVenus (a-GFP, yellow), constitutive mKate2 (a-RFP, green) along with stains for nuclei (DAPI, blue) and mucus (UEA-1, orange). Zoomed in sections of selected regions are shown as maximum projection of 2.5 μm z-stacks. In F) arrows indicate examples of individual bacteria labelled in both constitutive and inducible reporter channels. H-J) Maximum projection of 75 μm z-stack from selected regions as shown in E-G above. IHC targeting inducible mVenus (a-GFP, yellow) and constitutive mKate2 (a-RFP, green) is shown. K) Average intensity of inducible mVenus fluorescence channel (a-GFP IHC) for proximal and distal colon from bacteria segmented using constitutive mKate2 fluorescence level (a-RFP IHC). Graph shows individual datapoints and geometric mean ± geometric SD from the full tiled area of proximal colon shown in E-G and full tiled distal colon from same mouse. Statistics show results from one-way ANOVA with Tukey multiple comparison correction. *** = $p<0.005$, ****=$p<0.0001$. L) Average intensity of inducible mVenus channel (a-GFP IHC) in proximal colon as for K, analysed on concentric regions of the gut, from 0 (attached to the mucosa) to 3 (the most internal luminal area). Graph shows individual datapoints and geometric mean ± geometric SD mean. Statistics shown for Kruskal Wallis test with Dunn's multiple comparison adjustment as measured between treatments shown. ****= $p<0.0001$. M) Average intensity of inducible mVenus channel (a-GFP IHC) in proximal colon as for K, analysed on longitudinal sub-regions of the image from 0 (the most proximal side) to 3 (the most distal side). Graph shows individual datapoints and geometric mean ± geometric SD. Statistics shown for Kruskal Wallis test with Dunn's multiple comparison adjustment as measured between treatments shown. ****= $p<0.0001$.

For bacterial detection, dissected segments from proximal and distal colon were fixed, labelled with α-GFP (mVenus), α-RFP (mKate2), DAPI (nuclei) and *Ulex europaeus* agglutinin I (UEA-1) lectin, which binds α-linked fucose residues on glycoproteins and glycolipids (mucus), and cleared using the modified Ce3D method (Figure 4E-J; Supplementary Figure 5A-C). Individual bacteria labelled with both constitutive and induced reporters demonstrated the ability to detect bioreporter activity using this method (Figure 4F, single channel zooms). Tiled single-plane imaging across larger regions of the gut (Figure 4E-G) and 3D z-stack imaging of smaller regions (Figure 4H-J; Supplementary Figure 5A-C) showed clear increases in inducible reporter labelling in DSS treated animals compared with both healthy control and sialic acid inhibitor treated animals.

To quantify labelling differences in these samples, tiled images were segmented using a LABKIT classifier [36] to identify bacterial-sized particles labelled in the constitutive reporter channel. Quantification of inducible reporter labelling (Figure 4K) mirrored other inflammatory markers (Figure 4C-D), with considerable increases in average sialic-acid inducible reporter level in DSS-treated animals and a less elevated response in animal treated with both DSS and Neu5ac2en sialidase inhibitor (Figure 4K). Samples from both proximal and distal colon demonstrated similar patterns of response, but with increased signal detected in proximal DSS treated samples compared to distal (Figure 4K).

To determine whether the entire gut contents was required to reach sound biological conclusions we therefore analysed sub-regions of images from the Ce3D cleared samples tested in Figure 4. Reporter levels were broadly similar between all radial (Figure 4L, Supplementary Figure 6A) and longitudinal (Figure 4M, Supplementary Figure 6B) subsections, validating that robust assessment of reporter levels is possible using smaller populations of engineered bacteria and with less onerous imaging methods in this instance. Consistent with the decrease in inducible reporter response noted in the distal colon, this analysis also suggested progressively decreasing response within longitudinal subsections of the proximal colon in DSS treated animals (Figure 4M).

Longitudinal spatial profiling of sialic acid availability

To more deeply assess sialic acid response, we therefore delivered DTR413 bacteria to mice (n = 4 per group) as previously, with or without 3% DSS in drinking water and with or without daily Neu5Ac2en sialic acid inhibitor gavages and analysed sialic acid across the entire length of the mouse colon (Figure 5A). Disease progression and biosensor response was monitored via daily faecal sampling and via gut dissection at day 4 post bacterial and DSS administration. As expected, faecal CFU counts were similar between all groups (Figure 5B), and body weight and LCN-2 measurements at day 4 were indicative of disease impact in DSS treated animals that was mitigated by sialidase inhibition (Figure 5C-D).

Despite the challenges of direct detection of sialic acid, to allow comparison between methods we attempted to measure sialic acid levels in gut contents using both enzymatic detection kits (Figure 5E) and by gas-chromatography mass spectrometry (GC-MS; Figure 5F). Free sialic acid levels detected in faecal samples were indistinguishable between treatment groups when using either method (Figure 5E-F). Analysis of regional sialic acid levels in the gut was complicated by variability

in the amount and consistency of digesta between animals and treatment groups. Nevertheless, when digesta samples were extracted from broad regions of the gut (cecum, proximal and distal halves of the colon) and measured via GC-MS, there was a suggestion of elevated sialic acid levels specifically in the proximal colon of DSS treated animals similar to our whole-mount imaging results (Figure 5G).

For longitudinal imaging analysis, dissected gut samples were prepared as 'swiss-rolls' (Figure 5H). Sectioned samples were stained for constitutive (mKate2) and sialic acid inducible (mVenus) reporters, along with nuclei (DAPI) and neutrophils (Ly-6G/Ly-6C) and whole colons were imaged via confocal microscopy (Figure 5I-K). Images were then analysed in three equal sub-sections: proximal, mid, and distal colon (Figure 5I-K). Inducible reporter levels conclusively confirmed our tentative findings from whole-mount cleared imaging and GC-MS analyses, with increased sialic acid response detected in DSS treated samples when tested in the absence of concurrent sialidase inhibition (Figure 5I-Ki-iii; Figure 5L). Notably, reporter response in the proximal colon was significantly higher than in the mid and distal colon in these DSS treated animals (Figure 5I).

Surprisingly, when neutrophil infiltration was observed in the same sections, counts were consistently elevated in DSS treated animals within the mid-colon region, with limited indication of polymorphonuclear cell clusters in proximal and distal colon of DSS treated animals, nor at any sites in control or DSS + sialidase inhibitor treated groups (Figure 5I-Kiv; Figure 5M). These results were mirrored by blinded disease severity scoring of hematoxylin and eosin (HE) stained adjacent sections (Figure 5N; Supplementary Figure 7A-C). Together our results suggest that there is spatial separation between the response by the microbiota to elevated sialic acid and the primary site of inflammatory injury within the gut. They also demonstrate the superior ability of an engineered biosensor to distinguish between regional sialic acid availability compared with direct GC-MS quantification.

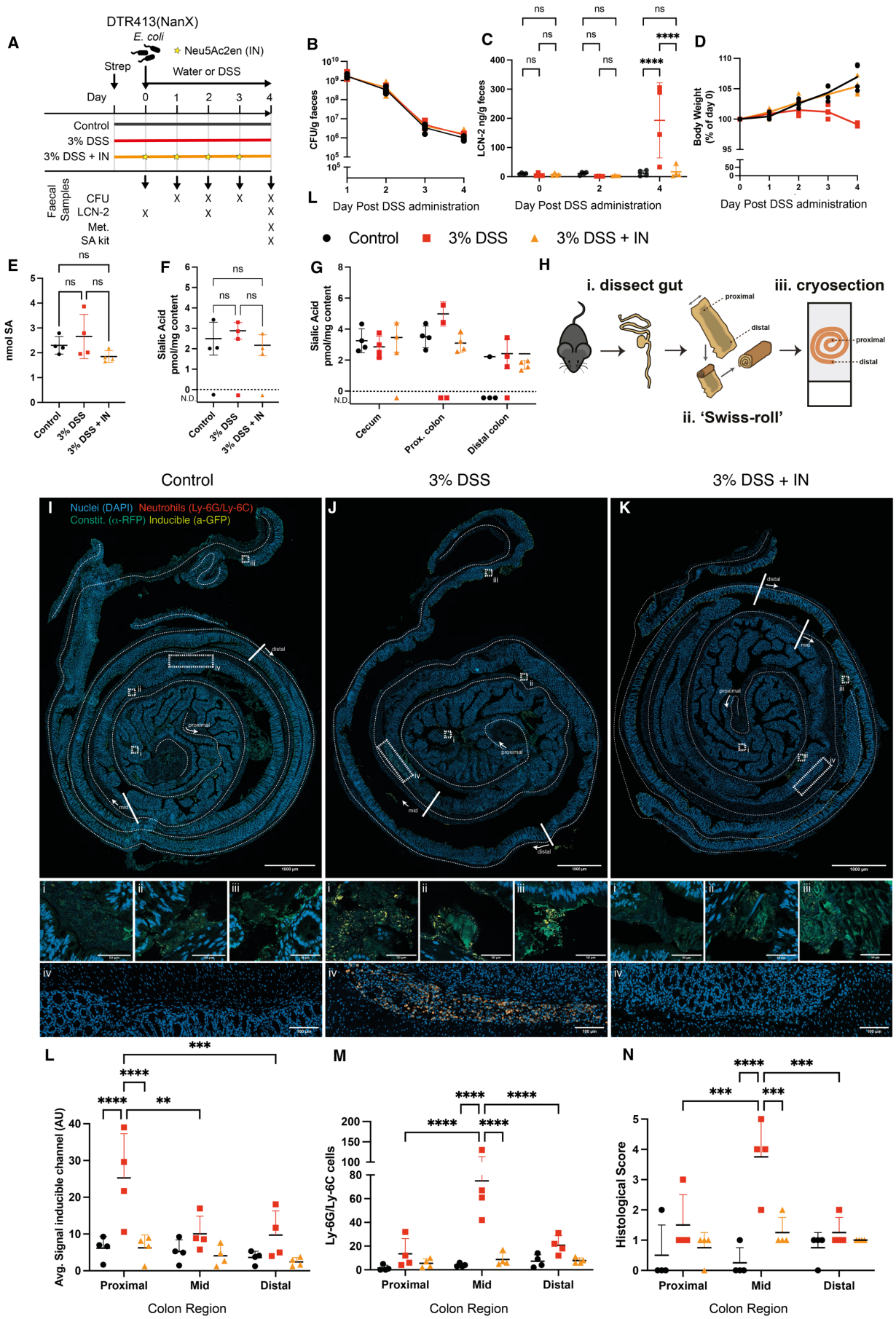
A
DTR413(NanX)
E. coli
Neu5Ac2en (IN)
Strep
Water or DSS
Day
Control
3% DSS
3% DSS + IN
Faecal Samples
CFU
LCN-2
Met.
SA kit
B
CFU/g faeces
Day Post DSS administration
C
LCN-2 ng/g feces
Day Post DSS administration
D
Body Weight (% of day 0)
Day Post DSS administration
Control
3% DSS
3% DSS + IN
E
nmol SA
F
Sialic Acid pmol/mg content
G
Sialic Acid pmol/mg content
Cecum
Prox. colon
Distal colon
H
i. dissect gut
ii. 'Swiss-roll'
iii. cryosection
proximal
distal
Control
3% DSS
3% DSS + IN
I
Nuclei (DAPI) Neutrohils (Ly-6G/Ly-6C)
Constit. (α-RFP) Inducible (a-GFP)
J
K
L
Avg. Signal inducible channel (AU)
Proximal
Mid
Distal
Colon Region
M
Ly-6G/Ly-6C cells
Proximal
Mid
Distal
Colon Region
N
Histological Score
Proximal
Mid
Distal
Colon Region

Figure 5. Longitudinal spatial availability of sialic acid during inflammation in a colitis mouse model. A) DTR413 sialic acid-inducible whole cell biosensors were administered to C57BL/6 mice (n = 4 per group) by gavage 24 hours following a single dose of streptomycin (5mg per mouse by oral gavage). DSS was administered from the day of bacterial delivery in the drinking water at 0% (control) and 3% with or without daily oral gavage of Neu5Ac2en sialidase inhibitor (IN; stars). B) DTR413 abundance was measured in faecal pellets collected daily post administration. C) LCN-2 levels, as quantified by indirect ELISA in faecal pellets collected at day 0, 2 and 4. Graph shows mean ± SD. Statistics show results from two-way ANOVA with Tukey multiple comparison correction between samples on each day as shown. ****=p<0.0001. D) Body weight change, expressed as a percentage of starting body weight of each mouse. Line shows mean. E) Concentration of sialic acid in faecal pellets at day 4 as analysed by enzymatic quantification kit. F) Concentration of sialic acid in faecal pellets at day 4 as analysed by GC-MS. G) Sialic acid concentration in caecum, proximal and distal colon at day 4 as analysed by GC-MS. Graphs E-G show mean ± SD. For E-F, statistics show insignificant differences from one-way ANOVA analysis with Tukey multiple comparison adjustment. For F-G, not determined (ND) values represent GC-MS chromatograms that failed quality control assessment and were excluded from further calculations; they are shown here for completeness only. H) Schematic of swiss-roll preparation of colon samples. I-K) Representative tile images of whole colon from I) Control, J) 3% DSS, and K) 3% DSS + IN treated animals. IHC labelling of inducible mVenus (α-GFP; yellow), constitutive mKate2 (α-RFP, green), and neutrophils (Ly-6G/Ly-6C, orange) along with nuclear staining (DAPI, blue) are shown. Annotations indicate the divisions used for longitudinal sections of proximal, mid and distal colon. Representative zooms of proximal (i), mid (ii) and distal colon (iii) for reporter-gene labelling, and mid colon for neutrophil infiltration detail (iv) are shown also. Scale bars are shown in figure. L) Geometric means of average signal of inducible mVenus reporter intensity (α-GFP) within bacteria segmented for constitutive (α-RFP) fluorochrome on swiss-roll sections of proximal, mid and distal colon at day 4. M) Neutrophil counts in gut regions based on a-Ly-6G/Ly-6C immunolabelling. N) Histological Score in each gut regions from blinded analysis of H&E labelled sections, combining a sum of independently scored changes in crypt architecture, inflammatory infiltrate, muscle thickening, goblet cell depletion and crypt abscess. For L-N, graphs show mean ± SD from 4 replicate animals. Statistics show results from two-way ANOVA tests with Tukey multiple comparison adjustment comparing experimental groups within a gut region and between gut regions within each experimental group. between groups. * = p<0.05, **=p<0.005; ***p<0.0005, ****p<0.0001.

Discussion:

Here we have combined engineered live microbial whole-cell biosensors with imaging to provide *in situ* spatial understanding of sialic acid bioavailability within the gut – an important pathway for host-microbe interactions and disease pathogenesis. Total sialylation levels in mammalian cells are increased in various inflammatory diseases [41,42] and increased gut microbial sialidase enzyme activity, which removes terminal sialic acids from glycoproteins, has also been implicated in disease pathogenesis [28]. However, detection of free sialic acid in the gut is complicated by its rapid utilisation by the microbiota. In contrast to traditional quantification attempts detailed here and by others, which poorly distinguish different disease states, our biosensor's response was strongly correlated with global measures of inflammatory disease severity and clearly separated between treatment groups (ie. control, DSS and DSS + sialidase inhibitor). This was the case despite detection relatively early in the onset of DSS-induced inflammation and thus at low total

inflammation levels. Our data point to free sialic acid as a potentially useful biomarker for global inflammatory disease status in the gut when it is sensed *in situ* by resident microbes.

Surprisingly, spatial analyses suggested regional segregation between sialic acid availability, which peaked within the proximal colon, and the primary impact site of colitis in the host, which peaked in the mid colon (Figure 5). This is of particular interest given that previous studies have implicated sialic acid induced *E. coli* blooms in the propagation of inflammation within the gut [28]. Our findings confirm a critical link in this pathway (Figure 1A) by measuring increased sialic acid levels during inflammation. At the same time, however, they point to an organ-wide mechanism of host-microbiome interaction that spatially segregates availability of a key inflammation-linked nutrient or microbes from the major site of inflammatory tissue damage. Aside from biological mechanism, these findings have important implications for the emerging field of engineered live bacterial diagnostics and therapeutics, particularly those that aim to induce therapeutic response specifically at the site of disease [43,44]. Indeed, sialic acid inducible circuits have been developed as prototype 'sense-and-response' systems for *in situ* delivery of therapeutics in antibiotic-induced inflammation [32]. Our results highlight that feedback mechanisms within the gut can occur across locations and thus the importance of spatial functional analyses for gaining a complete understanding of complex metabolic pathways in the gut for their use in engineered diagnostics and therapeutics.

A particular design focus in this study was the development of low-burden circuits with minimised reporter expression levels to achieve robust functionality when colonising the gut for extended periods. The engineered commensal *E. coli* NGF-1 biosensors developed here achieved effective colonisation following a single low dose of streptomycin, similar to previously developed synthetic systems using the same strain [39,40]. DTR413 bacteria remained functional while growing unselected in the mouse gut (Supplementary Figure 4C-E) and were able to report on sialic acid levels for at least 7 days, by which time these bacteria are at their stably maintained level (Supplementary Figure 4). This is a fundamentally different approach to whole cell biosensing than using the typical high-expressing, plasmid-based reporters dosed for immediate response. While reporter genes were expressed at lower levels than would typically be used, antibody labelling had the dual benefit of amplification and removing the dependence on fluorescent maturation which may be inconsistent in the variable oxygen environment of the gut. The functional stability of the sensor during extended growth within the gut (Supplementary Figure 4C-E), the large number of bacteria detected in images (Figure 4K) and the robustness of results to analysis of less particles

(Figure 4L-M) suggest the feasibility of future investigations over even longer periods and using lower bacterial abundances.

The optical clearance of gut tissues with the contents in place was successful and facilitated a complete view of gut bacteria in the context of the minimally perturbed host gut (Figure 3-4). Imaging at single bacterial resolution over ~cm tissue scale provides a spatial view of microbial response across populations and varying microenvironments. The compatibility of Ce3D clearing with various labelling and detection methods, including FISH labelling of bacterial species (Figure 3), demonstrates the ability to evaluate the microbiome using these tools and should facilitate more extensive spatial exploration of the host and microbiota during health and disease in future studies. This method therefore complements other powerful imaging techniques that have emerged to image bacteria within the context of the gut [45-47]. Here, however, we add the power of a reporter system to assess changes to the functional biogeography of the gut microbiome in addition to spatial ecological information.

The insensitivity of our results obtained from different radial sub-regions of whole-mount optically cleared samples (Figure 4L-M) is indicative of the relative dynamics of microbes between mucosal and luminal compartments over the time scales of sensor activation and fluorescent reporter maintenance in our specific engineered strain. This ultimately points to the robustness of this approach to metabolic pathway exploration and validates our use of the less resource-intensive imaging of mucus-associated microbes in swiss-roll samples for longitudinal correlation analyses. Other use cases, however, may vary more extensively on radial scales, and thus require analysis in whole mount samples.

The imaging of microbial transcriptional reporters is a generalisable approach to dissecting metabolic pathways involving host and microbiota. Given the microbiome's extensive sensing capacity, bacterial biosensors have been developed to detect a range of metabolites, and ongoing work in our laboratory and others aims to expand this repertoire [40,48]. Direct metabolite detection, especially in faeces, may be unrepresentative when metabolites are also utilised by host and/or microbiota. There are also practical limitations in sample collection from localised regions of the gut, with amount and consistency of digesta varying widely between individuals and with disease. Indeed, this is the most likely cause of 'not determined' values in several of our regional colon GC-MS samples (Figure 5). This fundamentally increases variability and limits utility of results. Conversely, biosensing in the context of a live member of the microbiota can offer insight into the

dynamics of availability for utilisation – driven by the complex interplay of localised metabolite production and utilisation. These tools promise to broaden the utility and understanding of key metabolites as biomarkers for health and disease – with potential utility both in research and the clinic.

Methods:

Bacterial strain construction

Details of all bacterial strains and plasmids developed for this study (Table S1) and primers used (Table S2) are provided. All synthetic circuits were integrated into the chromosome of the mouse commensal *E. coli* NGF-1 strain carrying a rpsL lys42arg mutation which affords high-level streptomycin resistance [34,49].

Constitutive fluorescence was achieved using an mKate2 variant, which includes 11 N-terminal residues from mCherry for increased translation [50], expressed downstream of either the synthetic J23101 promoter (https://parts.igem.org/Part:BBa_J23101) (DTR326) or the strong constitutive promoter pRNA-1 (all other strains). For integration in the genome, the pSL1521 pSPIN plasmid carrying the machinery for INTEGRATE mediated gene insertion [51] was modified to target the region between *rpnD (yjiP)* and *yjiR*. The choice of site was based on previous identification of this site as supporting high expression of an mCherry cassette without impacting *E. coli* growth [52]. The crRNA was designed to target a PAM site conserved between *E. coli* NGF-1, MG1655 and Nissle 1917 strains. The crRNA sequence was ordered as single stranded oligonucleotides (IDT) and duplexed by resuspending oligos at 200 µM in annealing buffer (100 mM potassium acetate; 30 mM HEPES, pH 7.5; IDT), mixing forward and reverse oligos in equal volumes and incubating at 95˚ C for 2 mins followed by gradual cooling to 25˚C over 45 minutes. The duplexed crRNA was then assembled into the pSL1521 vector by BsaI golden-gate assembly (GGA). pRNA1-mKate2 was amplified from LPT36 via PCR and J23101-mKate2 was ordered as a gBlock Gene Fragment (IDT), with both being assembled into the *rpnD-yjiR* targeted vector via HiFi assembly using manufacturer guidelines (NEB). Plasmids were first assembled in *E. coli* Dh5α, followed by miniprep and electroporation into *E. coli* NGF-1. Cells harbouring plasmids were grown overnight and colonies screened by PCR for genomic integration of fluorescent cassettes.

For rapid cloning of inducible mVenus constructs, promoters were assembled via SapI mediated GGA into pCR43, a modified Tn7 insertion vector derived from pGRG36 [53] via pCR06 [40] to facilitate GGA cloning of promoters to drive mVenus expression. Native *E. coli* promoters, chosen based on their predicted control via the transcriptional regulator NanR (*nanA, nanC, nanX and fimB*) using the Ecocyc database [54], were PCR amplified from *E. coli* NGF-1 gDNA using Q5 High-Fidelity PCR polymerase (NEB) following the manufacturer's guidelines. PCR primers with type IIS RE sites (SapI) for individual sensors were designed using Primer 3 in Geneious Prime (software version 2020.1.1-2023.1.1; Biomatters Ltd). PCR products were purified using a Monarch PCR Cleanup Kit (NEB) before GGA assembly. Synthetic promoters EB1, EB2, EB3 and EB4 [35] were ordered as ssDNA and duplexed as dsDNA with SapI overhangs before GGA. The tetracycline inducible strain DTR326 was cloned in a similar manner from SapI flanked PCR amplified TetR-P_{tet} promoter, however, also induced λ-cI gene in addition to mVenus and carried a λ-phage based memory system within the genome [49].

Reactions for GGA were set up with 3 nM of each DNA fragment component, 3 µL (15 units) of SapI, 0.25 µL (500 units) of T4 DNA Ligase, 2 µL of T4 DNA Ligase buffer and nuclease free water to a final volume of 20 µL. GGA reactions were cycled 30 times at 37°C for 5 minutes and 16°C for 5 mins, then stored at 4°C until transformation. 2 µL of the GGA mix was transformed into 50 µL of NEB 10-beta Competent E. coli (NEB) by heat shock according to the supplier's protocol and plated onto carbenicillin and streptomycin selective LB-agar plates. After positive colony PCR, plasmids were miniprepped (Monarch® Plasmid Miniprep Kit, NEB) and transformed into electrocompetent E. coli NGF-1 encoding constitutive mKate2 fluorescence (DTR328). Transformant plates were scraped with pre-warmed LB, pooled, diluted 1:1000 and grown for 6 hours at 30°C in LB-streptomycin-carbenicillin with 0.1% L-arabinose to induce Tn7-based genome integration. Cells were further back-diluted 1:1000 and grown overnight at 42°C three times in order to cure the now genome integrated biosensors of the circuit plasmids. Individually cloned sensors were confirmed by sanger sequencing (Eurofins) using primers flanking the Tn7 insertion site [53].

In vitro growth and induction of biosensor strains.

Unless otherwise noted, bacterial strains were grown individually at 37°C in LB broth or on LB agar plates. Where appropriate, streptomycin and carbenicillin were supplemented at 50 µg/mL and 200 µg/mL respectively.

For *in vitro* sialic acid induction, bacterial cultures were diluted 1:500 (LB media) or 1:100 (M9 media + 0.4% glycerol). 100µL of diluted cultures were added to a 96-well plate with a row of either LB or M9 media, depending on the assay. The inducer, N-(-)-Acetylneuraminic acid, 97% (Neu5Ac) was added either at the time of dilution or after 5 hours of growth depending on the assay. N-Acetyl-2,3-dehydro-2-deoxyneuraminic acid (Neu5Ac2en; sialidase inhibitor) or the same amount of PBS was added to the media in controls. Assays were performed in 96-well F-bottom black plates were covered with Breathe-Easy® sealing membrane (Sigma-Aldrich, Missouri, USA). On a CLARIOstar® Plus plate reader (BMG Labtech, Ortenberg, Germany), growing at 37°C, OD600 (optical density measured at a wavelength of 600nm) and fluorescence measurements (mVenus, Ex: 497-15/Em: 540-20; mKate2, Ex: 570-15/Em: 620-20) were taken every 15 mins with shaking between measurements. Fluorescence raw data was corrected for blank (media) by subtraction and normalised for OD600 and in some cases background fluorescence based on negative control strain DTR328 data to generate normalised fluorescence units. Fold change of normalised mVenus fluorescence was calculated based on the change of FU/OD600 at different concentrations of inducer within the same bacterial strain.

Mouse models

All animal experiments were carried out under approval of the local Ethical Review Committee according to UK Home Office guidelines. 5-7 weeks old female C57BL/6 mice were purchased from Charles River (UK). Mice were provided with Teklad 2019 Global Rodent Diet (Envigo), alfalfa free, to reduce autofluorescence of gut contents during imaging. Upon arrival, mice were randomly distributed according to the group size of each experiment, followed by at least a week of acclimatation to the diet and the facility.

E. coli NGF-1 engineered biosensor colonisation model

E. coli NGF-1 was administered as previously described [39,40]. Mice were administered 5mg of streptomycin sulphate (VWR, 0382-EU-50G) in 100µL PBS by oral gavage. Plating of PBS diluted faecal samples on streptomycin selective LB agar plates 24 hours post streptomycin gavage confirmed the absence of background streptomycin resistant bacteria in the mouse gut. E. coli strains were grown overnight in LB, washed twice in PBS and concentrated 1:20 (~10^{11} cells/mL). Mice were gavaged with 200 µL of the suspension. Bacterial load was estimated by serial dilution

and plating of freshly collected faecal pellets that were resuspended to 100 mg/mL in PBS and vortexed for 2 minutes.

Dextran sulfate sodium-induced colitis model

Mild-to-acute colitis was induced by oral administration of 1-3% DSS (36-50 kDa: MP Biomedicals) in the autoclaved drinking water of animals for 3 to 7 days depending on the experiment set up. To inhibit sialidase activity during DSS-induced colitis, 200 µL of N-Acetyl-2,3-dehydro-2-deoxyneuraminic acid (Neu5Ac2en) (10 mg kg-1 per day) was administered via oral gavage daily. Animals were monitored throughout the experiment for colitis severity through body weight, stool consistency and the presence of blood in faeces. At the end of the experiment, mice were humanely sacrificed, and the colons were retrieved for downstream analyses.

Anhydrotetracycline (aTc) induction model

For *in vivo* induction of the P_{tet} *E. coli* NGF-1 biosensor strain (DTR326), bacteria were prepared and gavaged as above. 24 hours post bacterial delivery, mice were gavage with a single dose of aTc (200 µL of 0.1 mg/mL in PBS). 6 hours post induction, mice were humanely sacrificed, and colon samples were retrieved for downstream analyses.

Routine evaluation of inflammation

Retrieved whole colons were measured in length to evaluate the impact of inflammation. Hema-screen™ Single Slides (Avantor-VWR) were used to qualitatively detect occult bleeding due to inflammation where indicated. Scoring was performed blinded.

Faecal lipocalin-2 (LCN-2) levels were quantified as previously [55]. Briefly, frozen faecal samples were reconstituted at 100 mg/mL in PBS containing 0.1% v/v Tween 20 and vortexed for 20 min to get a homogeneous suspension then centrifuged for 10 min at 12,000 rpm at 4°C. Clear supernatants were collected and stored at −20°C until analysis. LCN-2 levels were estimated in the supernatants by ELISA assay using the Duoset murine LCN-2 ELISA kit (R&D Systems) following the manufacturer's protocols.

Microbiota analysis

Faecal pellets (≈ 50 mg) were collected into 2ml microtubes with O-ring caps and stored at –80 °C. Prior to DNA extraction, samples were subjected to bead-beating by adding 100 mg of 0.1 mm zirconia beads and 1 ml of inhibiTEX buffer (Qiagen) to each tube. Samples were subjected to 3x 1 min bead-beating cycle using the Precellys Evolution homogenizer with 1 min rest on ice between. DNA extraction was then performed using QIAamp Fast DNA Stool Mini Kit as previously described [56].

For 16s rRNA sequencing, full length bacterial 16S rRNA genes (V1-V9) were amplified using PacBio forward (5'GCATC/barcode/AGRGTTYGATYMTGGCTCAG3') and reverse (5'GCATC/barcode/RGYTACCTTGTTACGACTT3') primers. DNA sample concentration was normalised at 500 pg/µL. KAPA HiFi HotStart 2x ReadyMix PCR was used for the reaction. Both the forward and reverse 16S primers were tailed with sample specific PacBio barcode sequences to allow for multiplexed sequencing. Barcoded 16S primers were arrayed into PCR plates using Echo acoustic liquid handler and the library was sequenced on Sequel IIe system on 1 SMRT cell 8M generating an average of 16,392 reads per sample (Q3: 20,765).

The PacBio sequencing data was processed using the nf-core/ampliseq pipeline, version 2.10.0 [57]. Within this pipeline, data quality was evaluated with FastQC [58], summarized with MultiQC [59], and primers were trimmed using Cutadapt [60]. Sequences were then examined as one pool (pseudo-pooled) using DADA2 to infer amplicon sequencing variants (ASVs). VSEARCH [61] was then used to cluster the ASVs with a pairwise identity of 0.97. Finally, taxonomic classification was performed by DADA2 and the database 'Silva 138.1 prokaryotic SSU' [62]. Clustered ASVs and taxonomic identifications were then analysed using R with the vegan package [63] to preform permutational analyses of variance (PERMANOVA), beta dispersion analyses and nonmetric multidimensional scaling (NMDS) ordination. Plots were generated using ggplot [64].

Sialic acid colorimetric assay kit in faecal pellets.

Determination of free sialic acid by colorimetric assay was conducted using a commercial kit (abcam, ab83375) following manufacture recommendations. Briefly, frozen faecal samples were reconstituted at 100 mg/mL in PBS containing 0.1% v/v Tween 20 and vortexed for 20 min to get a homogeneous suspension then centrifuged for 10 min at 12,000 rpm at 4°C. A standard curve for the colorimetric assay was set up from 0-10 nmol/well. Samples, Standards and background

controls were diluted in Assay Buffer IV/assay buffer 1:1 and mixed well with Reaction mix containing Sialic acid Converting Enzyme, Development Enzyme Mix/Sialic acid Development Mix and OxiRed Probe/Sialic acid Probe. Reactions were incubated 30 minutes protected from light. The output OD570nm was measured on a CLARIOstar® Plus plate reader. Calculations were performed based on the extrapolation values of the standard curve and presented as amount of free sialic acid in the sample well.

Gas Chromatography-Mass Spectrometry (GC-MS) of gut contents

Faecal pellets were extracted as previously described [65]; all solvents were Optima HPLC Grade (Fisher) unless otherwise stated. Briefly, 400 µL chloroform was added to the pellet and vortexed, followed by 200µL methanol and vortexed again. Samples were centrifuged (4°C, 10 min, 16,000 rpm), the supernatant transferred to a clean Eppendorf 1.5 mL tube and dried using a rotary vacuum concentrator (Christ; 10 mbar, 30°C). 600 µL methanol:water (2:1 v/v containing 1 nmol of *scyllo*-inositol as an internal standard) was added to the sample pellet, centrifuged (4°C, 10 min, 16,000 rpm), and transferred to the previous dried extract. Chloroform (133 µL) and water (200 µL) were added to the sample, vortexed vigorously, and centrifuged as before. The upper, aqueous fraction was transferred to a glass vial and dried using a rotary vacuum concentrator as above. The dried sample was washed with 30 µL methanol and dried again, with this wash step repeated once more.

Polar metabolites were derivatised for GC-MS analysis by adding 20 µL freshly prepared methoxyamine hydrochloride (20 mg/mL in pyridine, both Sigma), followed by brief vortexing and incubation at room temperature overnight. Next, 20 µL BSTFA + 1% TCMS ('TMS') reagent (Sigma) was added to each sample and incubated for >1 hour before injection of 1 µL onto the GC-MS.

Data acquisition was performed largely as previously described [66], using an Agilent 7890B-7000C GC-triple quadrupole MS system, using the following parameters: carrier gas, helium; flow rate, 0.9 mL/min; column, DB-5MS (Agilent); inlet, 270°C; temperature gradient was 70°C (2 min), ramp to 295°C (12.5°C/min), and ramp to 320°C (25°C/min, 3 min hold). Scan range was m/z 40-550. Data was acquired using MassHunter software (version B.10.0.384.1). Data analysis was performed using MANIC software, an in house-developed adaptation of the GAVIN package [67]. Qualitative analysis was performed using MassHunter Qualitative software (version 10.0). Metabolites were identified and quantified by comparison to authentic standards injected at the beginning and end

of the sequence. Calibration curves for sialic acid (SA) linearity was calculated from 1, 10, 25, 50 and 100 µM standard solutions.

Histological analysis of mouse colon

Swiss roll preparation of colon tissue was performed as previously described [68]. Dissected colon tissue was placed on parafilm, surrounding fat tissue was removed, and the organ was open longitudinally. Gently, faecal pellets at distal colon were removed with forceps, preserving the mucus and digesta before the tissue was flattened with the luminal side facing up. The proximal extremity of the colon was rolled towards the distal end and a small needle (30G) was used to pierce all colon layers and keep the tissue rolled-up. Rolled tissues were immediately fixed at RT using PBS containing 4% PFA for 4h. After fixation, samples were washed three times in PBS and immediately placed in 15% sucrose in PBS (6-12h until the tissue sank) before being transferred to 30% sucrose in PBS overnight. The organs were place in a cryomold with OCT embedding matrix, snap-frozen in 2-methylbutane over dry ice and stored at –80°C until cryosectioning was performed.

Cryosectioning of OCT embedded tissue was performed using a Leica cryostat. 20 µm sections were cut and mounted on SuperFrost Ultra Plus™ GOLD slides. Samples for immunohistochemistry and *in situ* Hybridisation were dried at RT for 10 min then fixed for 20 min in PBS containing 4% PFA follow by three washes to remove excess fixative.

Tissue for histological analysis was stained using hematoxylin (Mayer's, Sigma, Gillingham, UK) and eosin (CellPath, Newtown, UK). Blind Histological analysis of tissue sections was then graded by a board-certified veterinary pathologist of the Royal Veterinary College (London, UK) using light microscopy [69]. Crypt architecture (0-3), inflammatory cell infiltrate (0-3), muscle thickening (0-3), goblet cell depletion (0-1) and crypt abscess (0-1) were independently scored and added together to give the overall histological score for three longitudinal regions (proximal, mid and distal colon) of each animal.

Immunohistochemistry and FISH.

Fluorescence *in situ* hybridisation was adapted from previously described methods [70]. Briefly, fixed (4% PFA), three times washed (PBS) and permeabilised (PBS containing 0.15% v/v Triton X-100) sections were incubated in a hybridization buffer of 0.9 M NaCl, 0.02 M Tris pH 7.5, 0.01% SDS,

20% HiDi formamide and 2 µM probe at 46°C for three hours. The Eub338 probe, known to be effective over many, but not all, bacterial phyla [71] was custom synthesized and 5' labelled with Rhodamine Red X. After hybridisation, sections were washed three times at 48 °C for 10 minutes.

For immunolabelling, the tissue was washed twice in PBS and incubated for 15 min in PBS containing 0.15% v/v Triton X-100 for permeabilization. Samples were then incubated in blocking solution 45 min (PBS containing 5% v/v donkey serum) followed by primary antibodies diluted in blocking solution (1:200) for 1h at RT. Three washes in PBS ensued, before an incubation with secondary antibodies in blocking solution (1:500) for 45 min at RT. For those slides where conjugated agglutinins or lectins were used, an extra incubation time of 1 hour after the secondary antibody was included. After three washes to remove unbound antibody, PBS containing DAPI (1 µg/ml) was added for 10 min to label DNA. Finally, sections were washed three times in PBS and once with H2O before adding the mounting and closing the slides with coverslips. All antibodies and Fish probe are listed in Table S3.

Clearing enhanced 3D (Ce3D) analysis of murine gut tissue

For whole-mount analysis, dissected mouse proximal and distal colon samples were fixed without removing gut contents at RT using PBS containing 4% PFA for 4h. Once the tissue was fixed, samples were washed three times in PBS and placed in 15% sucrose in PBS (6-12h) for cryoprotection before being transferred to 30% sucrose in PBS overnight. Next day, tissue was embedded in OCT and cryopreserved at -80C. Samples were then cryosectioned using a Leica Cryostat, to remove the first ~200 µm and expose the lumen for more efficient penetration of antibodies/FISH probes. Samples were then washed gently in cold PBS to remove the excess of OCT matrix. Ce3D in mouse colon was adapted from the method of Li and colleagues [38]. A schematic of the workflow is presented in Fig. 3A. Incubation times, volumes and reagents were adapted depending on the tissue size, aiming to maintain the gut contents in place for analysis. All the steps were conducted at RT on a shaking gyro-rocker SSL3 protected from light exposure. Briefly, whole proximal and distal colon were placed 24-48h on a cryo-mold containing PLP buffer (2.5 ml of 4% PFA (v/v), 0.0212 g of NaIO4, 3.75 ml of L-lysine buffer, and 3.75 ml of P buffer). Then, samples were washed three times for two hours each in washing buffer (PBS containing 0.1% v/v Triton X-100 and 0.5% v/v 1-thiglycerol). Blocking and permeabilisation was performed during 12-24 h in blocking buffer (PBS containing 0.3% v/v Triton X-100, 1% BSA v/v and 5% v/v of donkey serum). FISH and immunolabelling were conducted as stated before, adapting incubation and

washing times for a major portion of tissue sample. To finalise fluorescence labelling, DAPI was added and incubated for 8 hours prior to a 24 h washing step, replacing washing buffer three times. Excess of washing buffer was gently removed, and samples were placed directly into one ml of freshly prepared Ce3D clearing solution in a cryomold protected from light for 7-10 days, replacing the Ce3D clearing solution every 48 h. Ce3D clearing solution was prepared based on the methods of Li and colleagues [38]. Briefly, 4 g of Histodenz were resuspended between 2 mL and 750 μL of 40% N-methylacetamide. 5 μL of Triton X-100 were added before mixing into a 37C shaking incubator during 24h. Once the mixing was completed, 25 μL L of 1-Thioglycerol were added to the solution that was mixed for 30 min more. After 7-10 days of clearing, proximal and distal colon were mounted individually onto a microscope slide using 3-4 gene frames to create a volume where the sample was placed with the luminal cryosectioned portion facing up. Ce3D was used as Mounting media and sealed with a cover slip no. 0. Once cleared, proximal and distal colon were mounted individually onto a microscope slide using 3-4 gene frames to create a volume where the sample was placed with the luminal cryosectioned portion facing up. Ce3D was used as Mounting media and sealed with a cover slip no. 0.

Microscopy analysis

In vitro activity of the sialic acid sensor, with and without antibodies, was evaluated in a Zeiss Axio Observer Widefield microscope with LED illumination, equipped with Plan Apo 100X/1.4 Oil Ph3 immersion objective, resolution 0,24 μm and controlled by Zen acquisition software and Hamamatsu Camera. The light Source was a Colibri 5/7, with LED 385 (32.1%) for DAPI, LED 475 (44.4%) for mVenus and LED 555 (60.5%) for mKate2 excitation.

Imaging of tissue samples was performed using a Leica SP8 inverted confocal microscope equipped with HCPL APO CS2 63X/1.40 Oil immersion objective (Resolution XY: 139.43; Resolution Z: 235.82; Free working distance: 140 μm), 4 Leica Lasers (Diode 405, Argon, DPSS 561, HeNe 594 and HeNe 633) and High sensitivity Detectors (HyD1, PMT2, HyD3 and PMT4).

Images were analysed using a combination of FIJI and Imaris softwares. Quantification of reported levels was performed using a segmentation classifier generated in Labkit (FIJI) [36]. The classifier was trained manually to distinguish between individual bacteria labelled for the constitutive fluorescence (mKate2) (all *in vivo* experiments) or based on DAPI labelled nuclei (*in vitro* experiments). Following a conservative approach, when clusters of bacteria could not be

segmented individually, those particles were not included in the analysis. Segmented particles of between 0.5-2 μm^2 were then used for average quantification of mVenus (*in vivo* experiments) or mVenus and mKate2 (*in vitro* experiments) signal. For illustration purpose, tile images were background subtracted 0.5 px, Gaussian blur 0.75 and Min/Max brightness adjusted in the same way for all samples within the experiment. Colour-blind friendly palettes were chosen based on the work of Okabe and Ito [72]. Z-stacks of regions of interest were shown as maximum projections of 2.5 μm or 75 μm, indicated on the legend of the figure. 3D reconstructions of the Z-stacks were generated using Imaris. Surfaces were created following identical parameters for all the samples.

Quantification and statistical analysis

Unless otherwise stated, statistical analyses were routinely performed by using GraphPad Prism (v10.0). Individual statistical tests along with correction for multiple comparisons used were chosen as appropriate to each dataset and are stated in the legend of each figure panel, accordingly.

Acknowledgements:

We thank Eleanor Herbert for assistance with histopathology and Marko Storch for assistance with Pacbio 16s sequencing. The *E. coli* NGF-1 strain used was a kind gift from Pamela Silver. pSL1521 (pSPIN, pSC101* backbone) was a gift from Samuel H. Sternberg (Addgene plasmid # 160729 ; http://n2t.net/addgene:160729 ; RRID:Addgene_160729). The pRNA1-mKate2 template LPT36 was a kind gift of Laurent Potvin-Trottier and Johan Paulsson. Imaging was performed at The Facility for Imaging by Light Microscopy (FILM) at Imperial College London. This research was funded by a Sir Henry Dale Fellowship to D.T.R (211230/Z/18/Z). C.M.R. was funded by a President's PhD Scholarship through Imperial College London.

Competing Interest Statement

The authors declare no competing interests.

References

1. Zeng, M.Y., Inohara, N., and Nunez, G. (2017). Mechanisms of inflammation-driven bacterial dysbiosis in the gut. Mucosal Immunol *10*, 18-26. 10.1038/mi.2016.75.
2. Schirmer, M., Strazar, M., Avila-Pacheco, J., Rojas-Tapias, D.F., Brown, E.M., Temple, E., Deik, A., Bullock, K., Jeanfavre, S., Pierce, K., et al. (2024). Linking microbial genes to plasma and stool metabolites uncovers host-microbial interactions underlying ulcerative colitis disease course. Cell Host Microbe *32*, 209-226 e207. 10.1016/j.chom.2023.12.013.
3. Tropini, C., Earle, K.A., Huang, K.C., and Sonnenburg, J.L. (2017). The Gut Microbiome: Connecting Spatial Organization to Function. Cell Host Microbe *21*, 433-442. 10.1016/j.chom.2017.03.010.
4. Eckburg, P.B., Bik, E.M., Bernstein, C.N., Purdom, E., Dethlefsen, L., Sargent, M., Gill, S.R., Nelson, K.E., and Relman, D.A. (2005). Diversity of the human intestinal microbial flora. Science *308*, 1635-1638. 10.1126/science.1110591.
5. Richard, M.L., Liguori, G., Lamas, B., Brandi, G., da Costa, G., Hoffmann, T.W., Pierluigi Di Simone, M., Calabrese, C., Poggioli, G., Langella, P., et al. (2018). Mucosa-associated microbiota dysbiosis in colitis associated cancer. Gut Microbes *9*, 131-142. 10.1080/19490976.2017.1379637.
6. Carstens, A., Roos, A., Andreasson, A., Magnuson, A., Agreus, L., Halfvarson, J., and Engstrand, L. (2018). Differential clustering of fecal and mucosa-associated microbiota in 'healthy' individuals. J Dig Dis *19*, 745-752. 10.1111/1751-2980.12688.
7. Jiao, L., Kourkoumpetis, T., Hutchinson, D., Ajami, N.J., Hoffman, K., White, D.L., Graham, D.Y., Hair, C., Shah, R., Kanwal, F., et al. (2022). Spatial Characteristics of Colonic Mucosa-Associated Gut Microbiota in Humans. Microb Ecol *83*, 811-821. 10.1007/s00248-021-01789-6.
8. Vaga, S., Lee, S., Ji, B., Andreasson, A., Talley, N.J., Agreus, L., Bidkhori, G., Kovatcheva-Datchary, P., Park, J., Lee, D., et al. (2020). Compositional and functional differences of the mucosal microbiota along the intestine of healthy individuals. Sci Rep *10*, 14977. 10.1038/s41598-020-71939-2.
9. She, J.J., Liu, W.X., Ding, X.M., Guo, G., Han, J., Shi, F.Y., Lau, H.C., Ding, C.G., Xue, W.J., Shi, W., et al. (2024). Defining the biogeographical map and potential bacterial translocation of microbiome in human 'surface organs'. Nat Commun *15*, 427. 10.1038/s41467-024-44720-6.
10. Shalon, D., Culver, R.N., Grembi, J.A., Folz, J., Treit, P.V., Shi, H., Rosenberger, F.A., Dethlefsen, L., Meng, X., Yaffe, E., et al. (2023). Profiling the human intestinal environment under physiological conditions. Nature *617*, 581-591. 10.1038/s41586-023-05989-7.
11. Vuik, F., Dicksved, J., Lam, S.Y., Fuhler, G.M., van der Laan, L., van de Winkel, A., Konstantinov, S.R., Spaander, M., Peppelenbosch, M.P., Engstrand, L., and Kuipers, E.J. (2019). Composition of the mucosa-associated microbiota along the entire gastrointestinal tract of human individuals. United European Gastroenterol J *7*, 897-907. 10.1177/2050640619852255.
12. Zhang, Z., Geng, J., Tang, X., Fan, H., Xu, J., Wen, X., Ma, Z.S., and Shi, P. (2014). Spatial heterogeneity and co-occurrence patterns of human mucosal-associated intestinal microbiota. ISME J *8*, 881-893. 10.1038/ismej.2013.185.
13. Muralitharan, R., Nakai, M.E., Snelson, M., Zheng, T., Dinakis, E., Xie, L., Jama, H., Paterson, M., Shihata, W., Wassef, F., et al. (2024). Influence of angiotensin II on the gut microbiome: modest effects in comparison to experimental factors. Cardiovasc Res *120*, 1155-1163. 10.1093/cvr/cvae062.

14. Gevers, D., Kugathasan, S., Denson, L.A., Vazquez-Baeza, Y., Van Treuren, W., Ren, B., Schwager, E., Knights, D., Song, S.J., Yassour, M., et al. (2014). The treatment-naive microbiome in new-onset Crohn's disease. Cell Host Microbe *15*, 382-392. 10.1016/j.chom.2014.02.005.
15. Dejea, C.M., Wick, E.C., Hechenbleikner, E.M., White, J.R., Mark Welch, J.L., Rossetti, B.J., Peterson, S.N., Snesrud, E.C., Borisy, G.G., Lazarev, M., et al. (2014). Microbiota organization is a distinct feature of proximal colorectal cancers. Proc Natl Acad Sci U S A *111*, 18321-18326. 10.1073/pnas.1406199111.
16. Saffarian, A., Mulet, C., Regnault, B., Amiot, A., Tran-Van-Nhieu, J., Ravel, J., Sobhani, I., Sansonetti, P.J., and Pedron, T. (2019). Crypt- and Mucosa-Associated Core Microbiotas in Humans and Their Alteration in Colon Cancer Patients. mBio *10*. 10.1128/mBio.01315-19.
17. Weiss, A.S., Niedermeier, L.S., von Strempel, A., Burrichter, A.G., Ring, D., Meng, C., Kleigrewe, K., Lincetto, C., Hubner, J., and Stecher, B. (2023). Nutritional and host environments determine community ecology and keystone species in a synthetic gut bacterial community. Nat Commun *14*, 4780. 10.1038/s41467-023-40372-0.
18. Grondin, J.A., Kwon, Y.H., Far, P.M., Haq, S., and Khan, W.I. (2020). Mucins in Intestinal Mucosal Defense and Inflammation: Learning From Clinical and Experimental Studies. Front Immunol *11*, 2054. 10.3389/fimmu.2020.02054.
19. Luis, A.S., and Hansson, G.C. (2023). Intestinal mucus and their glycans: A habitat for thriving microbiota. Cell Host Microbe *31*, 1087-1100. 10.1016/j.chom.2023.05.026.
20. Taniguchi, M., Okumura, R., Matsuzaki, T., Nakatani, A., Sakaki, K., Okamoto, S., Ishibashi, A., Tani, H., Horikiri, M., Kobayashi, N., et al. (2023). Sialylation shapes mucus architecture inhibiting bacterial invasion in the colon. Mucosal Immunol *16*, 624-641. 10.1016/j.mucimm.2023.06.004.
21. Robbe, C., Capon, C., Maes, E., Rousset, M., Zweibaum, A., Zanetta, J.P., and Michalski, J.C. (2003). Evidence of regio-specific glycosylation in human intestinal mucins: presence of an acidic gradient along the intestinal tract. J Biol Chem *278*, 46337-46348. 10.1074/jbc.M302529200.
22. Holmen Larsson, J.M., Thomsson, K.A., Rodriguez-Pineiro, A.M., Karlsson, H., and Hansson, G.C. (2013). Studies of mucus in mouse stomach, small intestine, and colon. III. Gastrointestinal Muc5ac and Muc2 mucin O-glycan patterns reveal a regiospecific distribution. Am J Physiol Gastrointest Liver Physiol *305*, G357-363. 10.1152/ajpgi.00048.2013.
23. Vimr, E.R., Kalivoda, K.A., Deszo, E.L., and Steenbergen, S.M. (2004). Diversity of microbial sialic acid metabolism. Microbiol Mol Biol Rev *68*, 132-153. 10.1128/MMBR.68.1.132-153.2004.
24. Almagro-Moreno, S., and Boyd, E.F. (2009). Insights into the evolution of sialic acid catabolism among bacteria. BMC Evol Biol *9*, 118. 10.1186/1471-2148-9-118.
25. Coker, J.K., Moyne, O., Rodionov, D.A., and Zengler, K. (2021). Carbohydrates great and small, from dietary fiber to sialic acids: How glycans influence the gut microbiome and affect human health. Gut Microbes *13*, 1-18. 10.1080/19490976.2020.1869502.
26. Bell, A., Severi, E., Owen, C.D., Latousakis, D., and Juge, N. (2023). Biochemical and structural basis of sialic acid utilization by gut microbes. J Biol Chem *299*, 102989. 10.1016/j.jbc.2023.102989.
27. Jennings, M.P., Day, C.J., and Atack, J.M. (2022). How bacteria utilize sialic acid during interactions with the host: snip, snatch, dispatch, match and attach. Microbiology (Reading) *168*. 10.1099/mic.0.001157.

28. Huang, Y.L., Chassard, C., Hausmann, M., von Itzstein, M., and Hennet, T. (2015). Sialic acid catabolism drives intestinal inflammation and microbial dysbiosis in mice. Nat Commun *6*, 8141. 10.1038/ncomms9141.
29. Kalivoda, K.A., Steenbergen, S.M., and Vimr, E.R. (2013). Control of the Escherichia coli sialoregulon by transcriptional repressor NanR. J Bacteriol *195*, 4689-4701. 10.1128/JB.00692-13.
30. Horne, C.R., Venugopal, H., Panjikar, S., Wood, D.M., Henrickson, A., Brookes, E., North, R.A., Murphy, J.M., Friemann, R., Griffin, M.D.W., et al. (2021). Mechanism of NanR gene repression and allosteric induction of bacterial sialic acid metabolism. Nat Commun *12*, 1988. 10.1038/s41467-021-22253-6.
31. Liang, Q., Ma, C., Crowley, S.M., Allaire, J.M., Han, X., Chong, R.W.W., Packer, N.H., Yu, H.B., and Vallance, B.A. (2023). Sialic acid plays a pivotal role in licensing Citrobacter rodentium's transition from the intestinal lumen to a mucosal adherent niche. Proc Natl Acad Sci U S A *120*, e2301115120. 10.1073/pnas.2301115120.
32. Koh, E., Hwang, I.Y., Lee, H.L., De Sotto, R., Lee, J.W.J., Lee, Y.S., March, J.C., and Chang, M.W. (2022). Engineering probiotics to inhibit Clostridioides difficile infection by dynamic regulation of intestinal metabolism. Nat Commun *13*, 3834. 10.1038/s41467-022-31334-z.
33. von Itzstein, M., Wu, W.Y., and Jin, B. (1994). The synthesis of 2,3-didehydro-2,4-dideoxy-4-guanidinyl-N-acetylneuraminic acid: a potent influenza virus sialidase inhibitor. Carbohydr Res *259*, 301-305. 10.1016/0008-6215(94)84065-2.
34. Ziesack, M., Karrenbelt, M.A.P., Bues, J., Schaefer, E., Silver, P., and Way, J. (2018). Escherichia coli NGF-1, a Genetically Tractable, Efficiently Colonizing Murine Gut Isolate. Microbiol Resour Announc *7*. 10.1128/MRA.01416-18.
35. Peters, G., De Paepe, B., De Wannemaeker, L., Duchi, D., Maertens, J., Lammertyn, J., and De Mey, M. (2018). Development of N-acetylneuraminic acid responsive biosensors based on the transcriptional regulator NanR. Biotechnol Bioeng *115*, 1855-1865. 10.1002/bit.26586.
36. Arzt, M., Deschamps, J., Schmied, C., Pietzsch, T., Schmidt, D., Tomancak, P., Haase, R., and Jug, F. (2022). LABKIT: Labeling and Segmentation Toolkit for Big Image Data. Frontiers in Computer Science *4*.
37. Li, W., Germain, R.N., and Gerner, M.Y. (2017). Multiplex, quantitative cellular analysis in large tissue volumes with clearing-enhanced 3D microscopy (C(e)3D). Proc Natl Acad Sci U S A *114*, E7321-E7330. 10.1073/pnas.1708981114.
38. Li, W., Germain, R.N., and Gerner, M.Y. (2019). High-dimensional cell-level analysis of tissues with Ce3D multiplex volume imaging. Nat Protoc *14*, 1708-1733. 10.1038/s41596-019-0156-4.
39. Riglar, D.T., Giessen, T.W., Baym, M., Kerns, S.J., Niederhuber, M.J., Bronson, R.T., Kotula, J.W., Gerber, G.K., Way, J.C., and Silver, P.A. (2017). Engineered bacteria can function in the mammalian gut long-term as live diagnostics of inflammation. Nat Biotechnol *35*, 653-658. 10.1038/nbt.3879.
40. Robinson, C.M., Carreño, D., Weber, T., Chen, Y., and Riglar, D.T. (2024). A discovery platform to identify inducible synthetic circuitry from varied microbial sources. bioRxiv, 2023.2010.2013.562223. 10.1101/2023.10.13.562223.
41. Sillanaukee, P., Ponnio, M., and Jaaskelainen, I.P. (1999). Occurrence of sialic acids in healthy humans and different disorders. Eur J Clin Invest *29*, 413-425. 10.1046/j.1365-2362.1999.00485.x.
42. Cheeseman, J., Kuhnle, G., Stafford, G., Gardner, R.A., Spencer, D.I., and Osborn, H.M. (2021). Sialic acid as a potential biomarker for cardiovascular disease, diabetes and cancer. Biomark Med *15*, 911-928. 10.2217/bmm-2020-0776.

43. Riglar, D.T., and Silver, P.A. (2018). Engineering bacteria for diagnostic and therapeutic applications. Nat Rev Microbiol *16*, 214-225. 10.1038/nrmicro.2017.172.
44. Robinson, C.M., Short, N.E., and Riglar, D.T. (2022). Achieving spatially precise diagnosis and therapy in the mammalian gut using synthetic microbial gene circuits. Front Bioeng Biotechnol *10*, 959441. 10.3389/fbioe.2022.959441.
45. Mondragon-Palomino, O., Poceviciute, R., Lignell, A., Griffiths, J.A., Takko, H., and Ismagilov, R.F. (2022). Three-dimensional imaging for the quantification of spatial patterns in microbiota of the intestinal mucosa. Proc Natl Acad Sci U S A *119*, e2118483119. 10.1073/pnas.2118483119.
46. Mark Welch, J.L., Hasegawa, Y., McNulty, N.P., Gordon, J.I., and Borisy, G.G. (2017). Spatial organization of a model 15-member human gut microbiota established in gnotobiotic mice. Proc Natl Acad Sci U S A *114*, E9105-E9114. 10.1073/pnas.1711596114.
47. Shi, H., Shi, Q., Grodner, B., Lenz, J.S., Zipfel, W.R., Brito, I.L., and De Vlaminck, I. (2020). Highly multiplexed spatial mapping of microbial communities. Nature *588*, 676-681. 10.1038/s41586-020-2983-4.
48. Schmidt, F., Zimmermann, J., Tanna, T., Farouni, R., Conway, T., Macpherson, A.J., and Platt, R.J. (2022). Noninvasive assessment of gut function using transcriptional recording sentinel cells. Science *376*, eabm6038. 10.1126/science.abm6038.
49. Kotula, J.W., Kerns, S.J., Shaket, L.A., Siraj, L., Collins, J.J., Way, J.C., and Silver, P.A. (2014). Programmable bacteria detect and record an environmental signal in the mammalian gut. Proc Natl Acad Sci U S A *111*, 4838-4843. 10.1073/pnas.1321321111.
50. Potvin-Trottier, L., Lord, N.D., Vinnicombe, G., and Paulsson, J. (2016). Synchronous long-term oscillations in a synthetic gene circuit. Nature *538*, 514-517. 10.1038/nature19841.
51. Vo, P.L.H., Ronda, C., Klompe, S.E., Chen, E.E., Acree, C., Wang, H.H., and Sternberg, S.H. (2021). CRISPR RNA-guided integrases for high-efficiency, multiplexed bacterial genome engineering. Nat Biotechnol *39*, 480-489. 10.1038/s41587-020-00745-y.
52. Goormans, A.R., Snoeck, N., Decadt, H., Vermeulen, K., Peters, G., Coussement, P., Van Herpe, D., Beauprez, J.J., De Maeseneire, S.L., and Soetaert, W.K. (2020). Comprehensive study on Escherichia coli genomic expression: Does position really matter? Metab Eng *62*, 10-19. 10.1016/j.ymben.2020.07.007.
53. McKenzie, G.J., and Craig, N.L. (2006). Fast, easy and efficient: site-specific insertion of transgenes into enterobacterial chromosomes using Tn7 without need for selection of the insertion event. BMC Microbiol *6*, 39. 10.1186/1471-2180-6-39.
54. Keseler, I.M., Gama-Castro, S., Mackie, A., Billington, R., Bonavides-Martinez, C., Caspi, R., Kothari, A., Krummenacker, M., Midford, P.E., Muniz-Rascado, L., et al. (2021). The EcoCyc Database in 2021. Front Microbiol *12*, 711077. 10.3389/fmicb.2021.711077.
55. Chassaing, B., Srinivasan, G., Delgado, M.A., Young, A.N., Gewirtz, A.T., and Vijay-Kumar, M. (2012). Fecal lipocalin 2, a sensitive and broadly dynamic non-invasive biomarker for intestinal inflammation. PLoS One *7*, e44328. 10.1371/journal.pone.0044328.
56. Lim, M.Y., Park, Y.S., Kim, J.H., and Nam, Y.D. (2020). Evaluation of fecal DNA extraction protocols for human gut microbiome studies. BMC Microbiol *20*, 212. 10.1186/s12866-020-01894-5.
57. Straub, D., Blackwell, N., Langarica-Fuentes, A., Peltzer, A., Nahnsen, S., and Kleindienst, S. (2020). Interpretations of Environmental Microbial Community Studies Are Biased by the Selected 16S rRNA (Gene) Amplicon Sequencing Pipeline. Front Microbiol *11*, 550420. 10.3389/fmicb.2020.550420.
58. Andrews, S. (2010). A Quality Control Tool for High Throughput Sequence Data. http://www.bioinformatics.babraham.ac.uk/projects/fastqc/.

59. Ewels, P., Magnusson, M., Lundin, S., and Kaller, M. (2016). MultiQC: summarize analysis results for multiple tools and samples in a single report. Bioinformatics *32*, 3047-3048. 10.1093/bioinformatics/btw354.
60. Martin, M. (2011). Cutadapt removes adapter sequences from high-throughput sequencing reads. 2011 *17*, 3. 10.14806/ej.17.1.200.
61. Rognes, T., Flouri, T., Nichols, B., Quince, C., and Mahe, F. (2016). VSEARCH: a versatile open source tool for metagenomics. PeerJ *4*, e2584. 10.7717/peerj.2584.
62. Quast, C., Pruesse, E., Yilmaz, P., Gerken, J., Schweer, T., Yarza, P., Peplies, J., and Glockner, F.O. (2013). The SILVA ribosomal RNA gene database project: improved data processing and web-based tools. Nucleic Acids Res *41*, D590-596. 10.1093/nar/gks1219.
63. Oksanen, J., Simpson, G., Blanchet, F., Kindt, R., Legendre, P., Minchin, P., O'Hara, R., Solymos, P., Stevens, M., Szoecs, E., et al. (2024). vegan: Community Ecology Package.
64. Wickam, H. (2016). ggplot2: Elegant Graphics for Data Analysis (Springer-Verlag New York).
65. Ding, S., Schoenmakers, I., Jones, K., Koulman, A., Prentice, A., and Volmer, D.A. (2010). Quantitative determination of vitamin D metabolites in plasma using UHPLC-MS/MS. Anal Bioanal Chem *398*, 779-789. 10.1007/s00216-010-3993-0.
66. MacRae, J.I., Dixon, M.W., Dearnley, M.K., Chua, H.H., Chambers, J.M., Kenny, S., Bottova, I., Tilley, L., and McConville, M.J. (2013). Mitochondrial metabolism of sexual and asexual blood stages of the malaria parasite Plasmodium falciparum. BMC Biol *11*, 67. 10.1186/1741-7007-11-67.
67. Behrends, V., Tredwell, G.D., and Bundy, J.G. (2011). A software complement to AMDIS for processing GC-MS metabolomic data. Anal Biochem *415*, 206-208. 10.1016/j.ab.2011.04.009.
68. Le Naour, J., Montégut, L., Joseph, A., Garbin, K., Vacchelli, E., Kroemer, G., Pol, J.G., and Maiuri, M.C. (2022). Improved Swiss-rolling method for histological analyses of colon tissue. MethodsX *9*, 101630. https://doi.org/10.1016/j.mex.2022.101630.
69. Kim, J.J., Shajib, M.S., Manocha, M.M., and Khan, W.I. (2012). Investigating intestinal inflammation in DSS-induced model of IBD. J Vis Exp. 10.3791/3678.
70. Hasegawa, Y., Mark Welch, J.L., Rossetti, B.J., and Borisy, G.G. (2017). Preservation of three-dimensional spatial structure in the gut microbiome. PLoS One *12*, e0188257. 10.1371/journal.pone.0188257.
71. Daims, H., Bruhl, A., Amann, R., Schleifer, K.H., and Wagner, M. (1999). The domain-specific probe EUB338 is insufficient for the detection of all Bacteria: development and evaluation of a more comprehensive probe set. Syst Appl Microbiol *22*, 434-444. 10.1016/S0723-2020(99)80053-8.
72. Okabe, M., and Ito, K. (2008). Color universal design (CUD): How to make figures and presentations that are friendly to colorblind people. https://jfly.uni-koeln.de/color/#pallet.

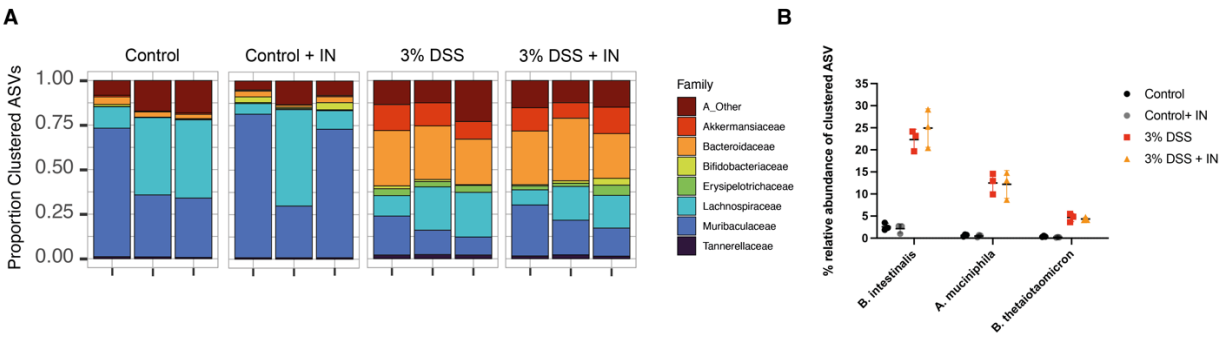

Supplementary Figure 1. A) Proportion of bacterial clustered ASVs within a family taxonomic classification at day 6. K) Percentage of relative abundance of clustered ASVs that showed similarity (over 97%) with those of *B. intestinalis*, *A. muciniphila* and *B. thetaiotaomicron* at day 6.

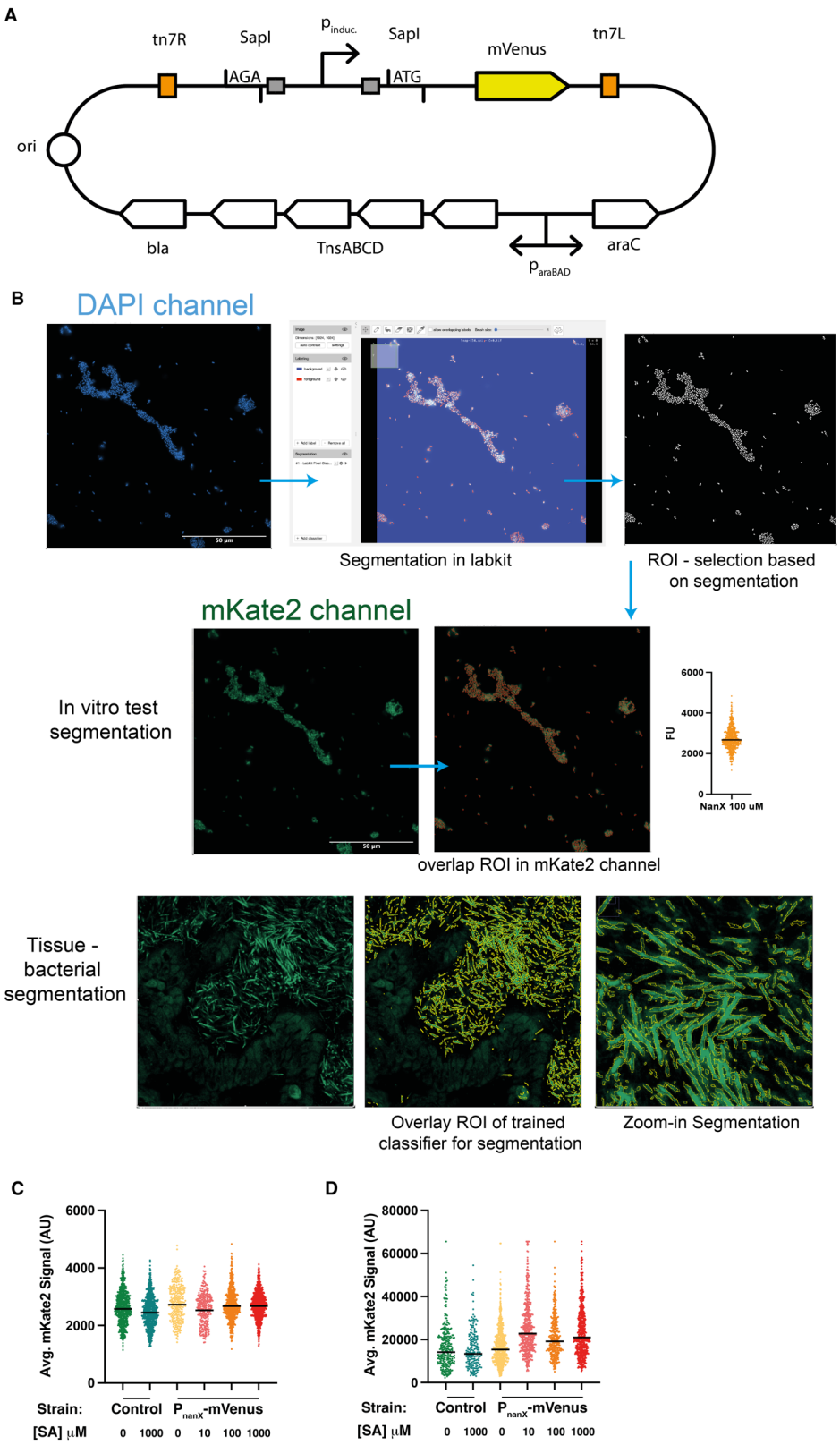

Supplementary Figure 2. A) Plasmid circuit design for genome integration of inducible promoters described in Figure 4. B) Workflow of segmentation analysis in Labkit software, FIJI. Training of classifier to create a selection ROI and overlay on the channel for average intensity analysis on the segmented areas. Tissue-bacterial segmentation, an example of the same Labkit classifier used in a cleared samples from Figure 3B. C) Average intensity signal of mKate2 at different Neu5ac concentrations at 6h growth in the negative control (DTR328) and NanX (DTR413) evaluated by widefield microscopy as shown in Figure 2F. D) Average intensity of mkate2 signal labelled with antibody (a-RFP) at increasing SA concentrations of 6h growth in the negative control (DTR328) and NanX (DTR413) evaluated by widefield microscopy as shown in Figure 2H.

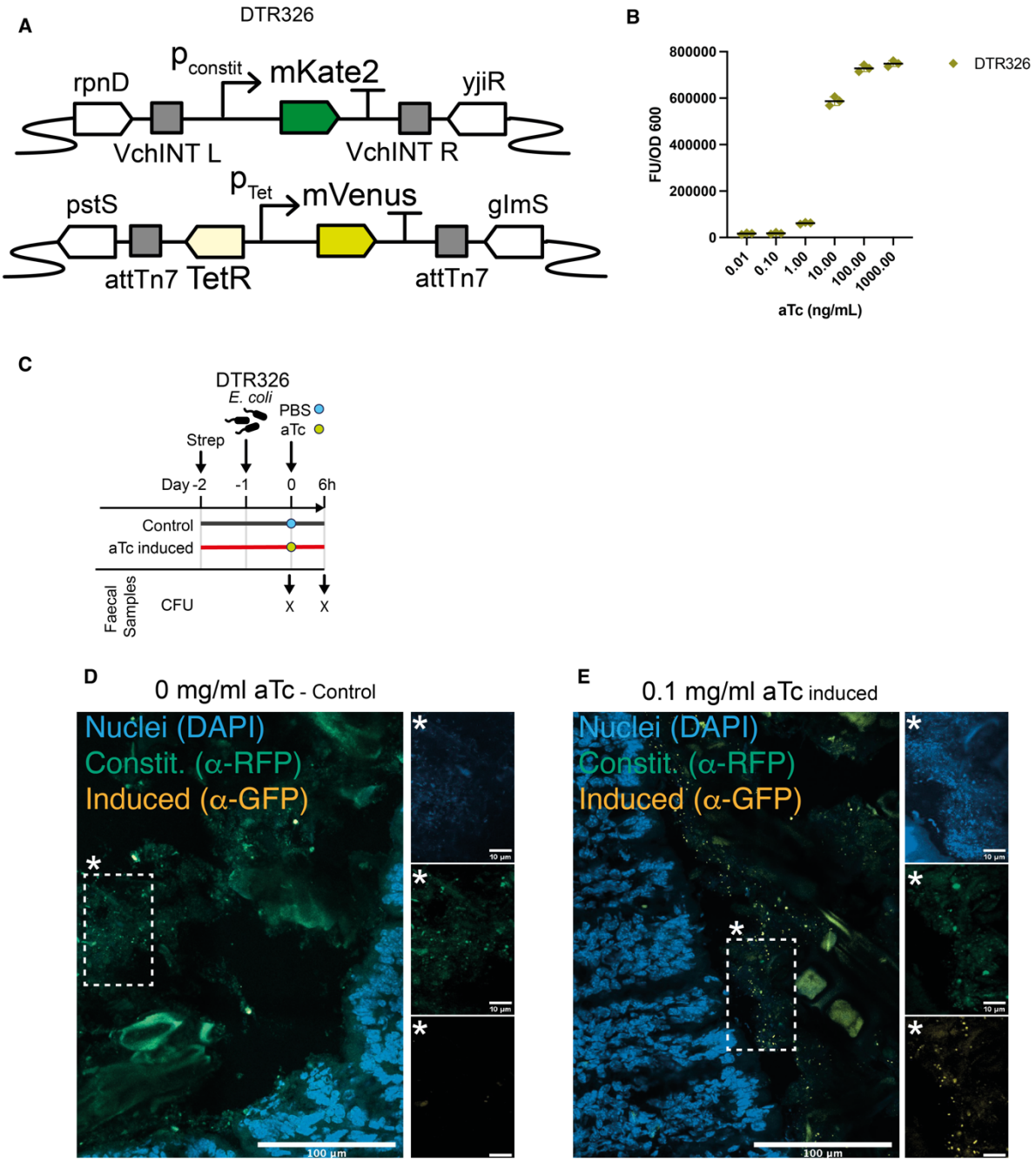

Supplementary Figure 3. A) Gene circuit construction of a tetracycline-induced whole cell biosensor (DTR326) as referred to in Figure 5C. B) Fluorescence mVenus output normalised by OD600 at 6 hours exposed to different concentrations of aTc in DTR328. Graph shows mean of 3 replicates. C) Set up of mouse experiment (C57BL/6, n=2 per group). Mice received DTR326 *E. coli* by oral gavage. The day after, a single dose of PBS or aTc was gavaged 6 hours before the end of the experiment. D-E) Detection of *in situ* induction of a tetracycline-based *E. coli* biosensor (DTR326) by imaging of Ce3D cleared mouse colon in D) the absence and E) the presence of anhydrotetracycline (aTc). Images show tiled region and zooms from sections with constitutive mKate2 labelled with IHC (green), inducible mVenus labelled with IHC (yellow) and DAPI labelled nuclei (blue). Scale bars as shown on images.

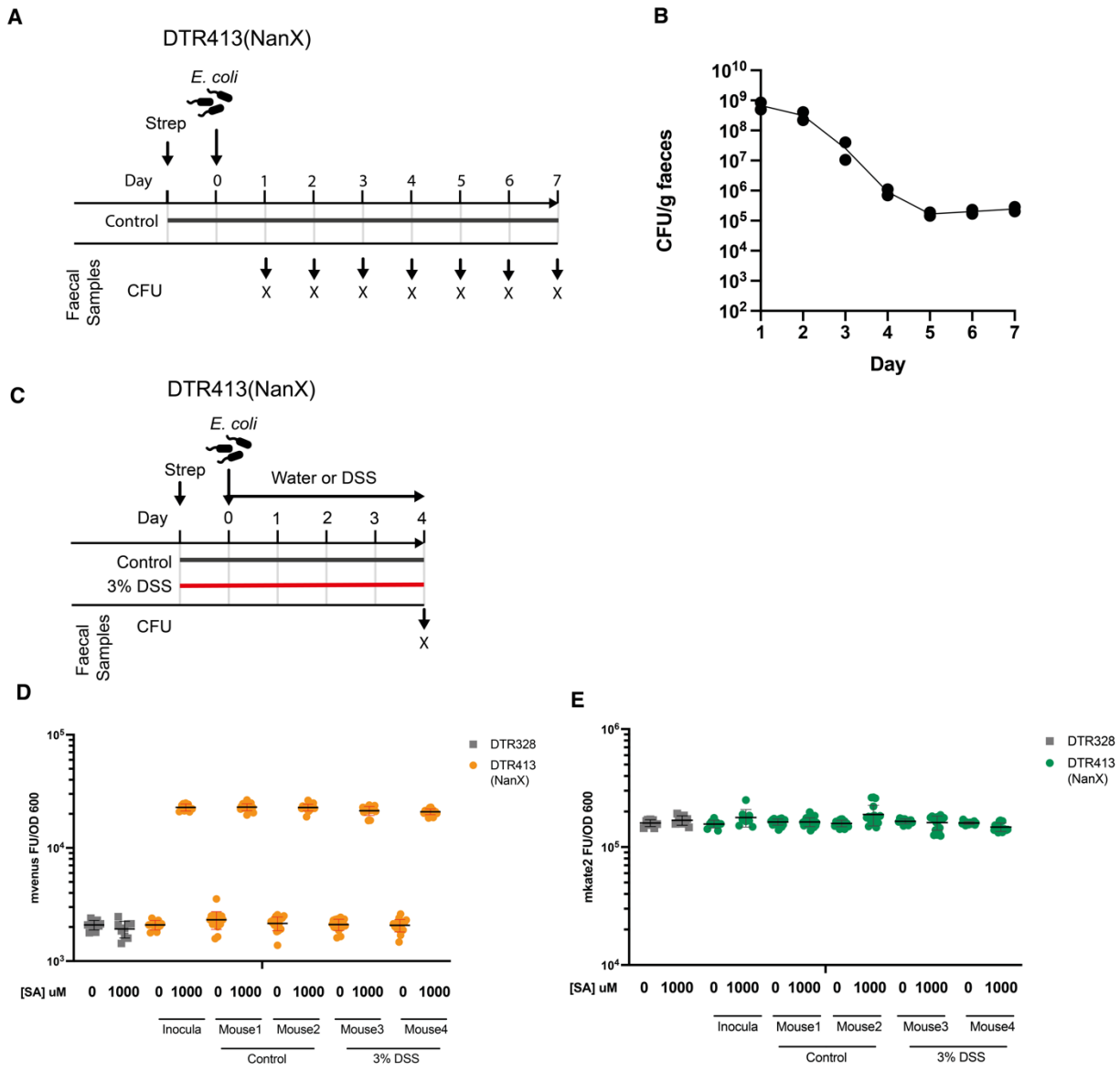

Supplementary Figure 4. A) DTR413 sialic acid-inducible whole cell biosensors were administered to C57BL/6 mice (n = 2 per group) by gavage 24 hours following a single dose of streptomycin (5mg per mouse by oral gavage). B) CFU counts from faecal pellets across the experiment. C) Set up of the mouse experiment (C57BL/6, n=2). Mice received DTR413 (NanX) by oral gavage a day after streptomycin treatment to aide colonization. DSS was administered from the day of bacterial delivery in the drinking water at 0% (control) and 3%. Faecal samples were collected at day 4. Average signal of mVenus/OD600 (D) and mKate2/OD (E) of individual colonies recovered from panel C post induction in LB media supplemented for 6 h with or without Neu5Ac (SA). Line shows mean of n=18 per mouse, compared to average signal fluorescence of n=9 replicates of DTR328 (negative control) and DTR413 (inocula).

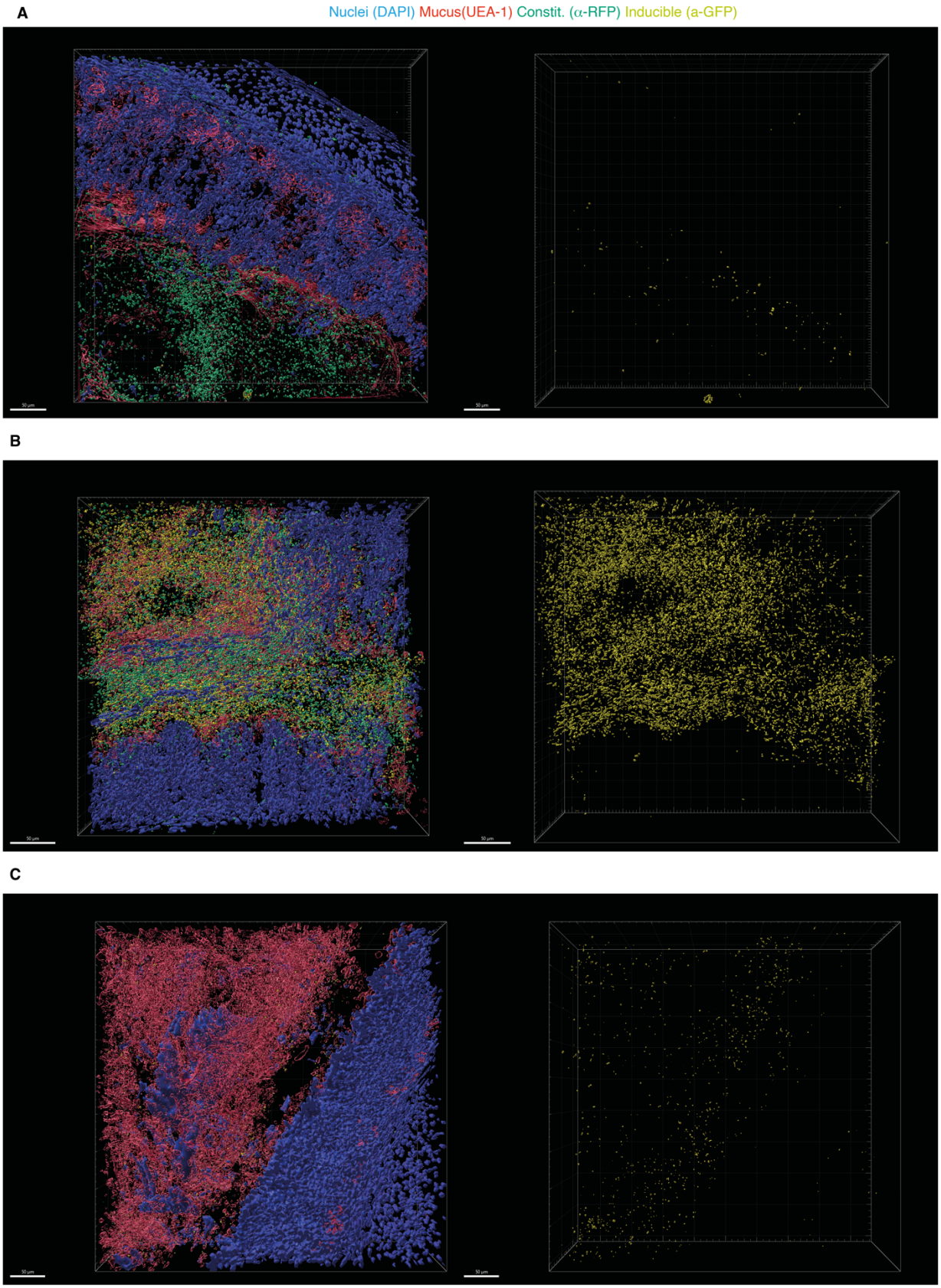

Supplementary Figure 5. A) 3D reconstruction in IMARIS of Z-stacks of 75 uM thickness of whole mount Ce3D samples of proximal colon in the Control (A), 3% DSS (B) and 3% DSS + IN (C) as in Figure 6F-H. Colours in overlays (left) correspond to a-GFP (mVenus, yellow), a-RFP (mKate2, green), DAPI (nuclei, blue) and *Ulex europaeus* agglutinin I lectin (UEA-1, vermillion). An individual representation of sialic-inducible mVenus, yellow, is also shown (right).

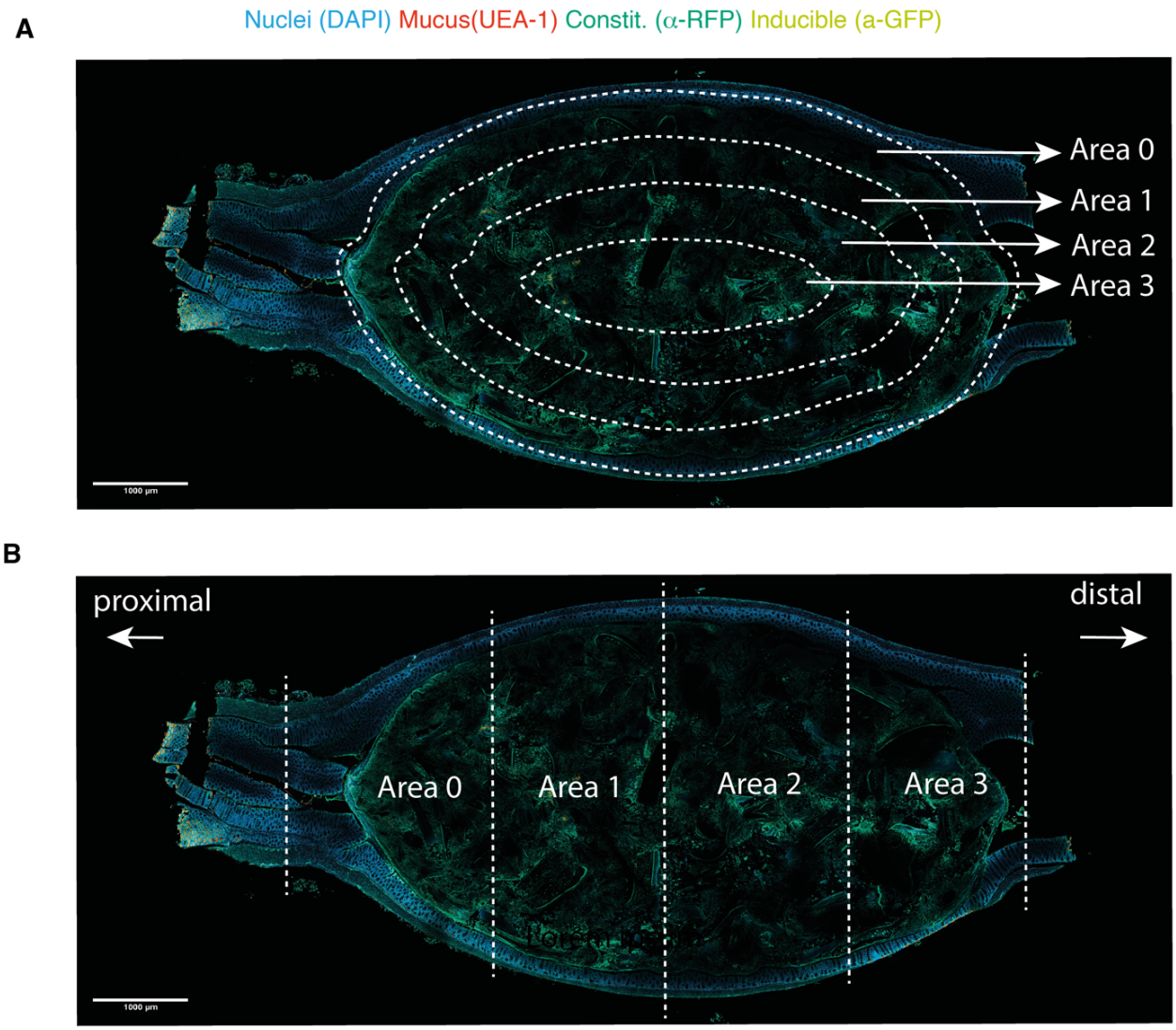

Supplementary Figure 6. A) Representation of the concentric analysis of areas from mucosa to the central luminal area shown in Figure 6L. Area 0 corresponds to the area attached to the mucosa layer and 3 the most internal luminal area. B) Representation of longitudinal analysis of areas from proximal to distal within the proximal colon cleared sample shown in Figure 6M. 0 corresponds to the most proximal side of the proximal colon and 3 the most distal side.

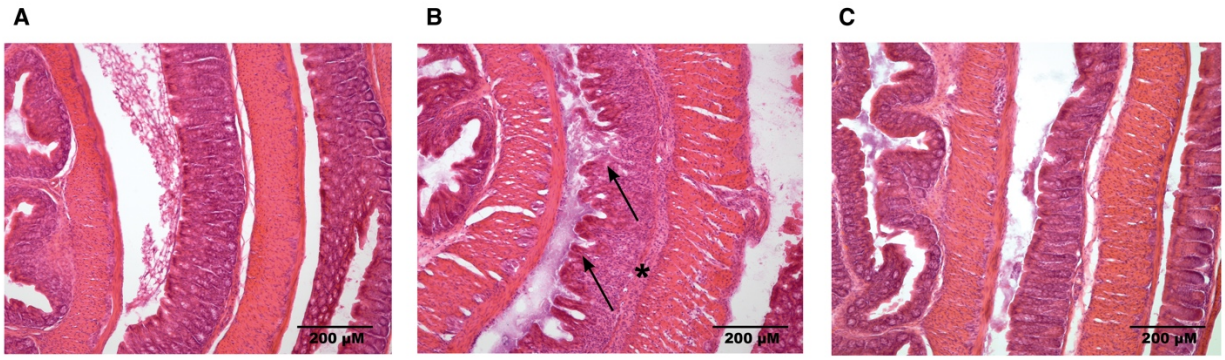

Supplementary Figure 7. Representative H&E staining of Swiss-roll sections at the mid colon of Control (A), 3% DSS (B) and 3% DSS + IN (C) as used for histological scoring in Figure 7K. Arrows indicate Changes in crypt architecture and * highlight cellular infiltration in the submucosa. Scale bars are shown on the image.

Supplementary Table 1. Bacterial strains and plasmids.

Strain	Genotype	Source
E. coli NGF-1	*rpsL K42R*	Kotula et al. (2014). Proc. Natl. Acad. Sci. U.S.A.
DTR326	*E. coli* NGF-1 *rpsL K42R;* attTN7::TetR-PtetA-cIDN-mVenus; attVchCAST (*rpnD-yjiR*)::PJ23101-mKate2; attIVchCAST(*lac)::*lambda-memory	This work
DTR328	*E. coli* NGF-1 rpsL K42R; attVchCAST(rpnD-yjiR)::PRNA1-mKate2	This work
DTR411	DTR328 + P*nanA*-mVenus [*E. coli* NGF-1 rpsL K42R; attVchCAST(rpnD-yjiR) PRNA1-mKate2; attTN7::PnanA-mVenus	This work
DTR412	DTR328 + P*nanC*-mVenus [*E. coli* NGF-1 rpsL K42R; attVchCAST(rpnD-yjiR) PRNA1-mKate2; attTN7::PnanC-mVenus	This work
DTR413	DTR328 + P*nanX*-mVenus [*E. coli* NGF-1 rpsL K42R; attVchCAST(rpnD-yjiR) PRNA1-mKate2; attTN7::PnanX-mVenus	This work
DTR414	DTR328 + PfimB-mVenus [*E. coli* NGF-1 rpsL K42R; attVchCAST(rpnD-yjiR) PRNA1-mKate2; attTN7::PfimB-mVenus	This work
DTR415	DTR328 + P*EB1*-mVenus [*E. coli* NGF-1 rpsL K42R; attVchCAST(rpnD-yjiR) PRNA1-mKate2; attTN7::PEB1-mVenus	This work
DTR416	DTR328 + P*EB2*-mVenus [*E. coli* NGF-1 rpsL K42R; attVchCAST(rpnD-yjiR) PRNA1-mKate2; attTN7::PEB2-mVenus	This work
DTR417	DTR328 + P*EB3*-mVenus [*E. coli* NGF-1 rpsL K42R; attVchCAST(rpnD-yjiR) PRNA1-mKate2; attTN7::PEB3-mVenus	This work
DTR418	DTR328 + P*EB4*-mVenus [*E. coli* NGF-1 rpsL K42R; attVchCAST(rpnD-yjiR) PRNA1-mKate2; attTN7::PEB4-mVenus	This work
Plasmids	**Description**	**Source**
pCR43	SapI compatible GGA destination vector for Tn7 - driven genome integration. attTn7-L - GGA site - mVenus - attTn7-R.	This work.
pCR06	SapI compatible GGA destination vector for Tn7 - driven genome integration. attTn7-L - GGA site - lambda-cI - CamR - attTn7-R.	Robinson et al. (2024). bioRxiv
pSL1521 pSPIN	Single plasmid V. cholerae CAST system (INTEGRATE). pSC101* backbone.	Vo et al. (2021). Nat Biotechnol.

Supplementary Table 2. Oligonucleotide and DNA Sequences

Oligo	Sequence
NanA-F	ATGCTCTTCTAGATTTAGTGAAGCAGATCG
NanA-R	TAGCTCTTCACATAAATACCTCTGAAGTG
NanC-F	ATGCTCTTCTAGAACTAGCTGTGCT
NanC-R	TAGCTCTTCACATAAATTTCACTCATTTGTAG
NanX-F	ATGCTCTTCTAGATGGTTCTGGTGTTTG
NanX-R	TAGCTCTTCACATATTTGTTTCCTGTGT
FimB-F	ATGCTCTTCTAGAAAGCAATACAAAGCC
FimB-R	TAGCTCTTCACATCGTTTTTCCCTTATAA
attTn7- SeqF	GATGCTGGTGGCGAAGCTGT
attTn7-SeqR	GATGACGGTTTGTCACATGGA
pCR43-SeqF	GGAACTAGATTTCACTTATCTGGTTGGTCG
pCR43- SeqR	TTTGTATAGTTCATCCATGCCATGT
DNA	**Sequence**
EB1 promoter	ATGCTCTTCTAGAGATTCGTTACCAATTGACAGCTACTGGTATAACAGGTATAAAGGTAGCTACTAGAATGTGAAGAGCTA
EB2 promoter	ATGCTCTTCTAGAGATTCGTTACCAATTGACAGCTACTGGTATAACAGGTATAAAGGTAGCTACTAGAGAAAGAGGAGAAATACTAGATGTGAAGAGCTA
EB3 promoter	ATGCTCTTCTAGAGATTCGTTCTGGTATAACAGGTATAAAGGTACTAGGTATAATGCTAGCTACTAGAGAAAGAGGAGAAATACTAGATGTGAAGAGCTA
EB4 promoter	ATGCTCTTCTAGAGATTCGTTCTGGTATGACAGGTATAAAGGTACTAGGTATAATGCTAGCTACTAGAGAAAGAGGAGAAATACTAGATGTGAAGAGCTA
rpnD-yjiR crRNA	TGGTCTCGATAATGATGCGCTACGCTTATCAGACCTACATTATCTGAACGAGACCT
J23101-mKate2	GTGATACATCCAGGTTGAGTAGCTCGAGTTTATTTTGACTAATAATGACCTACTTACCATGGGTATGGACAGTTTTCCCTTTGATATGTAACGCACGTTGTGGATATCTGGCGAAAATGAGACGTTTTACAGCTAGCTCAGTCCTAGGTATTATGCTAGCTAATAGAAATAATTTTGTTTAACTTTAAGGAGGTTTGGAATGGTTAGTAAAGGAGAAGAAAATAACATGGCACTGATTAAGGAGAACATGCACATGAAGCTGTACATGGAGGGCACCGTGAACAACCACCACTTCAAGTGCACATCCGAGGGCGAAGGCAAGCCCTACGAGGGCACCCAGACCATGAGAATCAAGGCCGTCGAGGGCGGCCCTCTCCCCTTCGCCTTCGACATCCTGGCTACCAGCTTCATGTACGGCAGCAAAACCTTCATCAACCACACCCAGGGCATCCCCGACTTCTTTAAGCAGTCCTTCCCTGAGGGCTTCACATGGGAGAGAGTCACCACATACGAAGACGGGGGCGTGCTGACCGCTACCCAGGACACCAGCCTCCAGGACGGCTGCCTCATCTACAACGTCAAGATCAGAGGGGTGAACTTCCCATCCAACGGCCCTGTGATGCAGAAGAAAACACTCGGCTGGGAGGCCTCCACCGAGACTCTGTACCCCGCTGACGGCGGCCTGGAAGGCAGAGCCGACATGGCCCTGAAGCTCGTGGGCGGGGGCCACCTGATCTGCAACTTGAAGACCACATACAGATCCAAGAAACCCGCTAAGAACCTCAAGATGCCCGGCGTCTACTATGTGGACAGAAGACTGGAAAGAATCAAGGAGGCCGACAAAGAGACTTACGTCGAGCAGCACGAGGTGGCTGTGGCCAGATACTGCGACCTCCCTAGCAAACTGGGGCACAGAGTCTAGCCTAGGACGTCCAAGCATCGTAGTGAGGTAA
TetR-Ptet	TTAAGACCCACTTTCACATTTAAGTTGTTTTTCTAATCCGCATATGATCAATTCAAGGCCGAATAAGAAGGCTGGCTCTGCACCTTGGTGATCAAATAATTCGATAGCTTGTCGTAATAATGGCGGCATACTATCAGTAGTAGGTGTTTCCCTTTCTTCTTTAGCGACTTGATGCTCTTGATCTTCCAATACGCAACCTAAAGTAAAATGCCCCACAGCGCTGAGTGCATATAATGCATTCTCTAGTGAAAAACCTTGTTGGCATAAAAAGGCTAATTGATTTTCGAGAGTTTCATACTGTTTTTCTGTAGGCCGTGTACCTAAATGTACTTTTGCTCCATCGCGATGACTTAGTAAAGCACATCTAAAACTTTTAGCGTTATTACGTAAAAAATCTTGCCAGCTTTCCCCTTCTAAAGGGCAAAAGTGAGTATGGTGCCTATCTAACATCTCAATGGCTAAGGCGTCGAGCAAAGCCCGCTTATTTTTTACATGCCAATACAATGTAGGCTGCTCTACACCTAGCTTCTGGGCGAGTTTACGGGTTGTTAAACCTTCGATTCCGACCTCATTAAGCAGCTCTAATGCGCTGTTAATCACTTTACTTTTATCTAATCTAGACATCATTAATTCCTAATTTTTGTTGACACTCTATCATTGATAGAGTTATTTTACCACTCCCTATCAGTGATAGAGAAAAGTGAA

Supplementary Table 3. Antibodies and FISH probe.

Antibody/FISH probe	Source	Catalog Number
Chicken IgY anti-GFP	Abcam	Cat# ab13970
Donkey anti-chicken IgY (H+L), highly cross-adsorbed, CF™ 488A	Sigma-Aldrich	Product # SAB4600031
Goat IgG anti-RFP	Cambridge Bioscience	Cat# 200-101-379S
Alexa Fluor 568 donkey anti-goat IgG (H+L)	Abcam	Cat # ab175704
Ulex Europaeus Agglutinin I (UEA I), DyLight® 649	Vector Laboratories	Cat# DL-1068-1
Ulex Europaeus Agglutinin I (UEA I), Fluorescein (FL-1061)	Vector Laboratories	Cat# DL-FL-1061
Rabbit IgG anti-MUC2 [EPR23479-47] - BSA and Azide free	Abcam	Cat # ab272706
Alexa Fluor 488 donkey anti-rabbit IgG (H+L)	Abcam	Cat # ab150061
Alexa Fluor 647 donkey anti-mouse IgG (H+L)	Abcam	Cat # a21202
Alexa Fluor 568 donkey anti-goat IgG (H+L)	Abcam	Cat # ab175704
Rat IgG anti-mouse Ly-6G/Ly-6C Monoclonal Antibody (RB6-8C5)	Invitrogen	Cat # MA1-10401
Alexa Fluor 647 donkey anti-rat IgG (H+L)	Abcam	Cat # ab150155
EUB338- FISH probe: /5RhoR-XN/GCTGCCTCCCGTAGGAGT	IDTdna	custom synthesized probe